_ANT UNDERSEA
_ARCH CENTRE
IORANDUM

AD-A200 680

Mixed layer deepening and variability in the upper layers of the central western Mediterranean, MILEX-82:

Final report

J. Moen

DTIC
ELECTE
NOV 2 3 1988
S   D

CdE

October 1988

Page count for SM-213
(excluding covers)

Pages	Total
i–iv	4
1–33	33
@1–@49	49
	86

SACLANT Undersea Research Centre
Viale San Bartolomeo 400
19026 San Bartolomeo (SP), Italy

tel: 0187 540 111
telex: 271148 SACENT I

NORTH ATLANTIC TREATY ORGANIZATION

Mixed layer deepening and
variability in the upper
layers of the central western
Mediterranean, MILEX-82:

Final report

J. Moen

Accession For

NTIS GRA&I	☒
DTIC TAB	☐
Unannounced	☐
Justification	

By

Distribution/

Availability Codes

| Dist | Avail and/or Special |
| A-1 | |

Issued by:
Underwater Research Division

J. Hovem
Division Chief

DTIC
ELECTE
NOV 2 3 1988
E

intentionally blank page

Mixed layer deepening and
variability in the upper layers of
the central western Mediterranean, MILEX-82:

Final report

J. Moen

Abstract: The 1982 Mixed-Layer Experiment (MILEX-82) is described
in detail and the data are presented in ways designed to illustrate the spa-
tial and temporal variability of the surface and deeper layers of the central
western Mediterranean, during the autumn transition period. The surface
mixed-layer is seen to cool and to deepen due to convection and mechanical
stirring induced by passing storms.

The predominating motions observed, and the ones given most attention
in this report, are the near inertial internal waves propagating horizontally
and vertically from the mixed layer into the pycnocline. Possible genera-
tion mechanisms for the vertical oscillations are discussed. It is argued that
these may originate well to the north of the study area in the Golfe du Lion,
where a high amplitude, inertially oscillating, Ekman mass-flux divergence
can be expected due to the high values of wind-stress curl in that region.

Data are, in some cases, fairly extensively 'worked up' to produce a vari-
ety of contour plots for temperature, salinity, density and dynamic anomaly
and a variety of composite time-series for both the thermistor-chain data
and current-meter array vectors. Also presented, but discussed in less de-
tail, are a number of measured and derived quantities relevant to air-sea
interaction and mixed layer deepening. It is considered that these will be
useful for comparison with other, similar experiments and with output from
numerical models.

Keywords: advection ○ air sea interaction ○ convection ○ current
meter ○ density ○ deep layer ○ Ekman mass-flux divergence ○ Golfe du
Lion ○ internal waves ○ Mediterranean ○ MILEX ○ mixed layer ○
modelling ○ pynocline ○ salinity ○ surface layer ○ surface mixing ○
temperature ○ thermistor chain ○ upwelling ○ vertical oscillation ○
wind stress curl

Contents

1. Introduction

A mixed-layer experiment (hereafter referred to as MILEX-82), designed to obtain a three-month coverage of the surface layer structure (upper 100 m) at one location, was begun in late September 1982 in the central western Mediterranean. Due to a combination of weather, mooring technique and instrumentation used (to be discussed later) the experiment had to be terminated earlier than planned, shortening the duration to just over one month. Fortunately, this was still a useful timespan for a mixed-layer experiment – since considerable mixing and deepening activity occurred throughout the period.

The purpose of MILEX-82 was threefold: firstly, to investigate the dominant processes responsible for surface layer mixing in the Mediterranean; secondly, to obtain a good data set against which to test and adapt one-dimensional numerical mixed-layer models; and thirdly, to complement the data gathered during the earlier MILEX-80 experiment in the north Tyrrhenian Sea.

It became evident during analysis of MILEX-80 data, described in Moen (1984), that one fairly important objective could not be adequately fulfilled: despite the overall quality of the data and the general success of the experiment, the complexity of the local oceanography made the MILEX-80 region unsuitable for the testing of one-dimensional mixed-layer models. Upwelling and horizontal advection tended to dominate vertical mixing in determining the depth of the mixed layer. Although gross estimates of upwelling were made from the data, they could not be separated from those of vertical mixing to the resolution necessary for one-dimensional model testing.

Thus it was hoped that MILEX-82 would provide data in which horizontal advection and upwelling were either effectively absent or, if present, completely resolvable due to proper choice of space and time sampling. Furthermore, the data were to be obtained under environmental conditions similar to those of MILEX-80, i.e. during the same season, and during similar air and sea temperatures, similar wind speeds, humidities, cloud covers, radiant heating and cooling conditions, and similar surface-layer stratifications. In this way a mixed-layer model 'tuned' to MILEX-82 conditions might be applied directly to MILEX-80 data for the purpose of separating the purely mixing influences on the mixed-layer depth from the purely dynamic.

It is important, from the military oceanography viewpoint, to recognize that the dynamics, in the form of upwelling and advection, are often more effective than mixing in determining the depth of the mixed layer. This is indeed the case for much of the Mediterranean where the wind stress is known to have a high spatial variability (as an example see Moen, 1984).

Another limitation of the MILEX-80 data, from the point of view of mixed-layer modelling, was its rather short duration of approximately three weeks. The longer time series of MILEX-82 will not only be more effective for model testing (not included in this report) but will also better resolve the influences of lower frequency effects on the surface layer. These effects had periods ranging from the inertial (18.66 h) to the passing of cyclonic lows (several days).

MILEX-82, then, was performed with the combined intentions of extending and complementing the data base of MILEX-80. It was conducted using mainly existing instrumentation and with the benefit of data preparation and analysis programs previously developed for MILEX-80.

The report therefore presents analyses of the MILEX-82 data and indicates their potential for comparison with mixed-layer models in a Mediterranean environment. Much of the interpretation of the data concerns the properties and effects of inertial oscillations in the mixed layer and thermocline.

2. Description of experiment

2.1. DEPLOYMENT OF INSTRUMENTS

Three thermistor-chain/current-meter moorings, marked A1, B1 and C1 in Fig. 1, were deployed in a triangular configuration of side 10 km with centre at 40°00'N, 006°00'E in the central western Mediterranean. The separation was chosen to correspond to the local Rossby radius of deformation and hence the expected length scale of variability at this location. Three additional current-meter moorings, marked A2, B2 and C2 in Fig. 1, were deployed within close proximity ($<$ 1 km) of A1, B1 and C1 respectively. All moorings, shown schematically in Fig. 2, were of the taut-nylon/surface-float type with the instruments arranged to span the surface mixed-layer and thermocline. Aanderaa meteorological chains were attached at 3.5 m to the surface floats of moorings B1 and C1. The position of each mooring is given by

A1: 39°56.00'N, 006°31.70'E
A2: 39°56.60'N, 006°31.90'E
B1: 40°00.01'N, 006°26.15'E
B2: 40°00.30'N, 006°25.20'E
C1: 40°02.10'N, 006°32.70'E
C2: 40°02.20'N, 006°32.90'E

The choice of spatial distribution for the moorings and instruments was influenced by two factors. Firstly, should they become important, first spatial derivatives at several different levels could be derived and hence crude estimates made there of horizontal advection and divergence. Secondly, should they *not be important* (i.e. in the absence of advection, divergence and strong horizontal gradients – which turned out to be the case), the moorings would be sufficiently close that horizontal separation could be ignored and greater vertical resolution obtained. In particular, such parameters as vertical shear, bulk gradient – Richardson number, and frequency, phase and energy of inertial oscillations could better be studied as a function of depth. Another advantage of the mooring configuration was in its duplication of measurements, particularly with regard to the thermistor and meteo-chains. This turned out to be well justified since three of the moorings came adrift in severe weather and the experiment had to be terminated much earlier than planned (see Sect. 2.2.).

2.2. DURATION OF EXPERIMENT

The moorings were deployed during the last week of September 1982 and recovered during the first week of November, with the longest records being of approximately 40 days duration. Figure 3 presents a timetable for each of the instruments, including times of XBT and CTD casts. Also shown in Fig. 3 are depths and sampling intervals for each of the moored instruments. In the case of the thermistor chains the depths refer to the uppermost and lowermost thermistors. Chains of 22 thermistors were formed by joining two 11-element Aanderaa thermistor chains end-to-end. The spacing allowed highest vertical resolution in the vicinity of what was guessed would be the mixed-layer/thermocline interface region as the mixed layer deepened. The depths of the thermistors are thus given relative to the uppermost progressing downwards, and relative to the lowermost progressing upwards, by the sequence 9.7, 12.7, 15.7, 18.7, 21.7, 24.7, 27.7, 32.7, 37.7 and 42.7 m.

Attached in-line to five of the moorings (see Fig. 2) were NBA current meters. This turned out to be an unfortunate oversight in the mooring design and the main reason for terminating the experiment early. It was suspected from measurements made during MILEX-80 that the NBA instrument might quite seriously over-estimate current speed when attached to a taut-nylon surface-mooring, but it was not suspected that the vertical oscillations of the mooring line could be so energetic as to snap the tension/tie bar of the current meter. It appears that (due to large direction vanes on its tail end) asymmetry of the drag forces on the current meter forced it to oscillate vertically, causing an upward or downward tilting of the instrument that pointed always into its direction of motion. Since this periodic tilting could be arrested only by the tension/tie bar passing through the centre of buoyancy of the current instrument, a critical stress occurred there -- causing the bar to fracture and snap. This stress was related to the energy and duration of the vertical oscillations, which in turn were related to the sea state and possibly were augmented through resonance of the stretched nylon rope with one of the lower frequency surface waves.

MILEX-82 took place in three phases: a mooring deployment phase, conducted by the SACLANTCEN research vessel *Maria Paolina G* during which XBT and CTD measurements were made on a grid as indicated in Fig. 1; a CTD/XBT survey phase (Fig. 4a) conducted by the Italian Navy hydrographic research vessel *Ammiraglio Magnaghi*, during which surveillance of the moorings was carried out; and an emergency recovery phase, again using the *Maria Paolina G*. It was indeed fortunate and invaluable to the experiment that the Italian Navy were in the vicinity during the period when moorings broke loose. This incident illustrates the importance of regular surveillance of surface moorings in open ocean experiments.

Recovery of the drifting moorings was greatly expedited through the assistance of the Italian Navy aircraft *Spada 1* (30th Air Squadron) in response to a request from SACLANTCEN to MARISTAT Rome. The ship's track for recovery of the moorings is indicated in Fig. 4b.

2.3. DATA RECORDING AND PREPARATION

Sampling intervals for each of the instruments are given in Fig. 3. These were 15 min for the vector averaging current meters (VACMs) and the thermistor chains, 6 min for the two surviving NBA current meters (NBA566 and 567) and 4 min for the two Niel-Brown acoustic current meters and for the vector measuring current meter (VMCM).

For the current meters, samples represent averages over the sampling interval, thereby effectively filtering out frequencies greater than $0.5t$, where t is the sampling interval. This is not so for the thermistor chains: as supplied by the manufacturer, they have a time-constant of 1 min, and so sampling at less than 1 cycle/min could cause aliasing. This problem was discussed in more detail in Moen (1984), where it was demonstrated that aliasing should not be serious providing sampling is at $\frac{1}{3}$ cycle/min or higher. In order to increase the thermistor time-constant, thermistors were wrapped using a 4.5 mm layer of PVC tubing and tape. The frequency response was tested by applying an impulse of finite width, which entailed (540 s) plunging the thermistor between two baths at different temperature and measuring the impulse response.

The response time series was digitised and Fourier transformed and the frequency response function H was calculated by the formula

$$H(f) = \frac{|G_{xy}(f)|}{|G_x(f)|},$$

where $G_{xy}(f)$ is the cross spectrum of the impulse x with the response y and $G_x(f)$ is the autospectrum of the impulse. Figure 5 is a plot of H which shows that at 4 cycles/h, the sampling frequency used, the thermistor response is less than 20%. Aliasing for the thermistor chain data was therefore not a problem.

Data from the moored instruments were recorded on magnetic cassettes, transcribed onto 8-track HP tapes, transferred to UNIVAC disc storage and then prepared for analysis by replacement of 'bad' data values and truncation. Onboard acquisition of XBT and CTD data was done by the SACLANTCEN IOS (Integrated Oceanographic System) on the Hewlett-Packard 21MX computer. Data were stored on 8-track HP tapes and later transferred to UNIVAC disc storage where they were 'cleaned' by removal of spikes and 'bad' profiles.

3. Spatial description

3.1. UPPER LAYER (ABOVE 150 m)

The MILEX-82 area, by contrast with that of MILEX-80, was found to contain relatively little horizontal variation in respect of thermodynamic variables.

■ *3.1.1. Temperature sections*

South-north and west-east temperature sections for the upper 150 m are presented in Fig. 6. They show that there is no large-scale horizontal structure in the south-north direction but in the west-east direction the thermocline rises appreciably as it approaches the shelf break to the west of Sardinia. The 23 °C isotherm, for example, which represents the mixed-layer/thermocline transition depth near the mooring triangle, rises from about 35 m, changing gradually at first, and then more rapidly until it reaches about 12 m near the shelf break. It would appear from the west-east section, therefore, that the depth of the potentially-mixed layer increases fairly rapidly from 0 to 30 m going westward from the Sardinian shelf. Just how rapidly is not possible to say due to the poor spatial resolution afforded by the two most eastward CTD stations 10 and 1 on Fig. 6b. It might, for example, be attributed to an internal near-surface front crossing somewhere between stations 10 and 1.

Although isotherms are bending upward towards the shelf, indicative of upwelling, the surface water there is actually warmer than that to the west. Such a situation could not prevail long, however, in the presence of strong winds – since in this case the surface water would cool quickly due to vertical mixing. Figure 6b thus provides an intersting example of when satellite infrared imagery would not reveal the underlying structure or dynamics. Upwelling would not be suspected in a zone where the surface temperature was seen to increase! Fortunately, this anomalously cold sub-surface water is far from the mooring sites, and so any associated dynamic effect or movement of the structure ought not to interfere with the one-dimensional mixing assumed to be taking place there. A better indication of the horizontal extent of the cold water is given by the 20 m horizontal section of Fig. 8a (discussed below).

■ *3.1.2. Salinity sections*

A slightly different picture emerges from the salinity transects shown in Fig. 7. The south-north section (Fig. 7a) indicates low salinity gradients crossing the mooring region, involving CTD stations 9, 6, 5 and 7, but a rather strong gradient develops

throughout the whole 150 m depth south of station 26. As will be argued later, this most likely corresponds to the northward branching loop of the North African current as it flows eastward from the Alboran Sea through the Sardinia Strait.

The west-east section (Fig. 7b) shows a surface gradient in salinity passing right through the MILEX-82 zone, strongest near the surface ($\sim$ 0.5 ppt/100 km) and becoming very weak by the 50 m level. Such salinity changes do not, however, translate to very strong density gradients, and since the variations are also very much a surface phenomena there are no important dynamics associated with them. One possible explanation is the following. Water slowly upwelling off the northwest Sardinia coast throughout the summer would tend to cause a shallower mixed layer there. Heating and evaporation would, in the absence of strong wind mixing, tend to concentrate heat and salt in the shallow layer more than in the deeper mixed layer to the west. Warmer saltier water could then spread slowly south-westward within the mixed layer due to Ekman transport.

3.1.3. Horizontal sections

Comparing horizontal sections of temperature (Fig. 8a) with salinity (Fig. 9a) at the 20 m level it is clear that the salinity maximum occurs to the west of the temperature minimum. The closed contours indicated in salinity, therefore, do not imply the existence of a gyre or eddy in that region. They might imply, instead, that the higher salinity, heavier surface water present above the doming isotherms is simply displaced westward and downward, where in horizontal section it shows up as a region of anomalously high salinity.

Comparing both the temperature (Fig. 8a) and salinity (Fig. 9a) maps at the 20 m level with potential density, contoured in the map of Fig. 10a, it is clear that at this level temperature has the dominant effect on density. Any important dynamics will be controlled far more by temperature than by salinity – a situation not abnormal for the Mediterranean surface layer. At the 200 m level, however, potential density (Fig. 10b) depends equally, if not more strongly, on salinity. Vertical sections of density have not been included since they appear virtually identical in form to those of temperature.

3.1.4. Geostropic currents

To examine at the dynamics of the MILEX-82 region we consider maps of dynamic anomaly calculated relative to motion at 1000 m. Two such maps are presented: Fig. 11a for 20 m (effectively surface) level and Fig. 11b for the 200 m level. Included also, for comparison, is a wintertime surface dynamic-topography map (Fig. 11c) reproduced from Ovchinnikov (1966).

It should be noted here that in common with all horizontal sections describing the MILEX-82 area, the contours suffer from an inadequate grid of CTD stations – particularly towards the extremities of the grid. Consequently, any interpretation of

the dynamics to the east near the colder water is difficult and somewhat subjective. There is a tendency for the contouring package to close contours going away from the grid region.

Although the MILEX-82 maps represent only one survey taken in the autumn period, whereas Ovchinnikov's map represents wintertime during the 1950s and was based on a coarser survey grid (0.5° squares), the two pictures show some agreement. In both maps, for example, part of the eastward flowing North African current loops to the north entering, the MILEX-82 zone at the southwest corner, turning southeastward and then leaving via the southeast corner. The MILEX-82 picture, however, indicates a high amplitude wave-like feature characterizing this flow both at the 20 m and 200 m levels. It has the appearance of being baroclinically unstable – especially at the 20 m level. The cyclonic flow looping into the northeast of the 20 m map is associated with the cold water (possibly upwelled) in that region shown on the temperature map (Fig. 8a). It is confined to the near-surface layer and can be regarded as a variation on the summertime picture (not shown, but stated by Ovchinnikov (1966) to be basically the same as the wintertime circulation).

On the basis of the dynamic anomaly map (Fig. 11a) the surface geostrophic current near the mooring sites (40°00'N, 006°30'E) was southward at about 7 cm/s. This geostrophic flow itself does not give rise to advective changes in the mixed-layer depth since the flow will be along isopycnal surfaces. Although other flow acting near the surface, such as Ekman transport and inertial oscillations, could produce advective changes to the mixed layer, the spatial gradients near the moorings, and for a large distance surrounding them, appear to be very weak. Advection effects on the mixed-layer depth are therefore assumed not to be important during MILEX-82.

3.2. INTERMEDIATE LAYER (150–1000 m)

Included less for their direct relevance to the sea surface mixed layer but more for their general interest value and for completeness, are south-north and west-east transects of temperature (Fig. 12a,b, respectively) and of salinity (Fig. 13a,b, respectively) for the deeper 150 m to 1000 m layer. These show the presence of the relatively salty (38.5 ppt), warm (13.4 °C) Levantine Water between the depths of about 300 and 650 m; a layer slightly deeper and thinner than that reported in the Ligurian Sea, for example, by Crepon, Wald and Monget (1982).

In the north-south direction this Levantine layer decreases in both temperature and salinity. The temperature decrease (Fig. 12a) is from about 13.5 °C to 13.3 °C, and the salinity decrease (Fig. 13a) is from 38.55 ppt to 38.50 ppt. Such fine anomalies apart, comparison of these transects with portions of similar transects presented in the Mediterranean Atlas of Miller, Tchernia and Charnock (1970) show good general

– 8 –

agreement for this layer. Small variations are only to be expected since the so-called Levantine-Water layer is highly variable throughout the Mediterranean.

Some weak temperature anomalies are also evident within the Levantine Water for the west-east section (Fig. 12b) but far more striking in this section are the warm and cold temperature 'blobs' sitting just above the Levantine layer. However, these are largely density compensated by salinity, and any remaining density anomalies could have no significant dynamic effect.

■ *3.2.1. Step structure*

Several of the CTD profiles taken to the west of the MILEX-82 zone displayed a pronounced step-like structure occurring mostly below the salinity maximum and within the Levantine layer as alternating relatively salty warm and fresh cool layers. As regards density, however, the profiles were usually less step-like. Two examples of the more pronounced step-like structure are shown in Fig. 14. In the case of CTD no. 8 an enlargement of the density profile is shown with an interpretation in terms of steps superimposed upon it. (No further discussion of these structures is presented.)

4. Thermistor chain data

4.1. ISOTHERM TIME SERIES SECTIONS

The thermistor chain pairs (upper and lower) for each mooring were combined as described in Sect. 2.2. Temperature contours were constructed by cubic spline interpolation between the 22 thermistors in the vertical and then linear interpolation in time (i.e. 15 min depth values for each isotherm were joined by straight-line segments). The resulting isotherms are displayed as 10-day sections in Fig. 15a,c for mooring A1, Fig. 16a,d for mooring B1 and Fig. 17a,d for mooring C1. The depths of uppermost and lowermost thermistors are marked in 24 h intervals on each section by a star symbol and a corresponding instantaneous temperature value. This avoided the problem of labelling contours and also allowed a greater density of them to be displayed. Isotherms are distinguished by simply counting in rounded half-degree intervals between printed temperatures. As a reference to mechanical forcing, the local wind speed is also plotted above each section in Figs. 15, 16 and 17. Several of the thermistors of the lower thermistor chain TC570 malfunctioned for much of the 35 days of measurement. These 'bad' data were replaced before contouring by cubic spline interpolations in depth by utilizing all the data points considered to be 'good'. Although great care was taken in interpolation the spiky appearance of the resulting isotherms (Fig. 17a,d) should be treated with some caution – especially since the other, relatively nearby, thermistor chains A and B do not display the same characteristic.

A limitation of the simple contouring method employed is its inability to cope with temperature inversions, although these were thought from preliminary examination to be unlikely, especially in the upper thermocline. The method was to search for isotherms beginning at the top and terminate search at the first occurrence of the required temperature value. If temperature inversions were present at mooring C they might also account for the confusing shape of the isotherms there. It is unlikely, however, that inversions would occur only at C and not at A and B.

4.2. INERTIAL OSCILLATIONS

We see from the isotherm displacement in Figs. 15 to 17 that the thermocline is characterized by strong inertial waves. The wave amplitudes were typically about 3 m or 4 m throughout most of the 35 days of measurements. They were greatest during stormy conditions following rapid increases in the wind speed such as oc-curred around days 279 and 280 and they appear to have been greater at mooring A (Fig. 15b) than at the other two moorings (cf. Figs. 16b and 17b). All the plots show a tendency for the amplitude to increase with depth; a good example being during the relatively calm weather, such as days 270 to 280 (Fig. 15a), when inertial waves can hardly be seen in the highly stratified water of the upper thermocline but are fairly pronounced lower down (amplitude of up to 5 m). The same effect occurred during the stormier conditions around days 280 to 284 (Fig. 15b) with amplitude increasing through the thermocline from about 6 to almost 9 m. The total energy of the vertical oscillations, however, may not be increasing with depth in the same way since the buoyancy restoring forces due to stratification are far higher in the upper than in the lower thermocline.

There appears to be a significant delay between increases in wind speed and the onset of vertical oscillations. A good example occurred between days 278 and 281 at mooring A (Fig. 15a,b). The wind increased fairly rapidly, starting about 6 h before day 279 at 1 m/s and reaching 16 m/s 9 h later. No corresponding response can be observed in the thermocline at this stage. Over the next 18 h the wind dropped back to 2 m/s and increased again to 13 m/s. Only then, some 24 h after the onset of these strong wind changes did the isotherms begin to respond. The oscillations began with a strong downward displacement of the isotherms and then continued to oscillate at near inertial frequency for about 6 days; by which time they had attenuated considerably.

4.3. GENERATION OF VERTICAL OSCILLATIONS

Why should there be such a delayed response of the thermocline to the winds? The answer will depend on which generation mechanism causes the vertical oscillations.

■ 4.3.1. Horizontal advection

The possibility of horizontal advection of sloping isotherms by currents can be dis-counted as a mechanism since there is no evidence of even weak thermal fronts during MILEX-82 (see Sect. 3.1). Indeed, were this to be the mechanism, we note that taking inertial circles to be of order 4 km diameter at the thermocline depth (a typical value taken from progressive vector diagrams not shown here) and tempera-ture changes of up to 4 °C per inertial cycle (Fig. 15b), a front as strong as 1 °C/km would be necessary to fully account for the observed vertical oscillations through advection. In any case, since little delay occurs between sudden wind changes and

– 11 –

the horizontal oscillations (see Fig. 23 of Sect. 5.1) such advective effects could not explain the delay in vertical oscillations.

The importance of advection should not be de-emphasized too strongly, however, since there is evidence from CTD data for spatial intermittance of temperature and salinity structures in the lower thermocline similar to those in the Levantine Water shown in Fig. 14 of Sect. 3. If such structures were present in the vicinity of mooring C, for example, their advection back and forth by the inertial currents might explain the abrupt changes and 'top-hat' shapes observed in the isotherms there (Fig. 17a,d – see also cautionary remarks concerning accuracy of these isotherms in Sect. 4.1). The shape of the vertical oscillations, at least, will certainly be modified by advective effects, although they do not constitute vertical motion.

There are essentially two theories on the direct forcing of vertical inertial oscillations and the consequent downward propagation of inertio-gravity waves. Both of these could account for the observed delay in thermocline response to the winds. The first, due to Kroll (1975), requires a mean Ekman mass flux divergence and hence spatial variations in the wind stress. The second, due to Kroll (1982) and Kroll (1984), involves a parametric instability of the slab-like mixed-layer flow and does not depend on spatial variations in wind stress.

■ 4.3.2. Spatially varying wind stress

To illustrate in a simple way how spatial variations in wind stress can induce vertical oscillations we write down the linearized, bulk (vertically integrated) momentum balance for the mixed layer reduced to the form

$$\frac{\partial \mathbf{U}}{\partial t} + f\hat{\mathbf{k}} \times \mathbf{U} + \frac{1}{\rho}\boldsymbol{\tau}_0 = 0, \tag{1}$$

where U and V are the bulk horizontal velocity components in an orthogonal coordinate system (x,y,z) with z directed $(+w)$ upward, f is the Coriolis parameter, $\hat{\mathbf{k}}$ is the unit vertical vector, and τ_x and τ_y are the surface wind stress components. A solution to Eq. (1) for a suddenly imposed wind stress describes the familiar inertial oscillations and Ekman mass transport for the mixed layer (Pollard et al., 1973). Taking the divergence and curl of Eq. (1) and using the continuity relation

$$\frac{\partial U}{\partial x} + \frac{\partial V}{\partial y} = w_{-h}, \tag{2}$$

where $z = -h$ is the mixed-layer base, yields

$$\frac{\partial w_{-h}}{\partial t} - f\,\text{curl}\,\mathbf{U} + \frac{1}{\rho}\,\text{div}\,\boldsymbol{\tau}_0 = 0$$

$$\frac{\partial}{\partial t}(\text{curl}\,\mathbf{U}) + fw_{-h} + \frac{1}{\rho}\,\text{curl}\,\boldsymbol{\tau}_0 = 0. \tag{3}$$

– 12 –

A solution to Eq. (3) for a suddenly imposed wind stress which then remains constant in time but varies spatially is given by

$$w_{-h} = \frac{-1}{f\rho} \operatorname{div} \boldsymbol{\tau}_0 \sin ft + \operatorname{curl} \boldsymbol{\tau}_0 (1 - \cos ft),$$

$$\operatorname{curl} \mathbf{U} = \frac{1}{f\rho} \operatorname{div} \tau_0 (1 - \cos ft) - \operatorname{curl} \boldsymbol{\tau}_0 \sin ft. \tag{4}$$

We see from Eq. (4) that vertical oscillations can arise due to either a purely divergent or a purely rotational wind stress. In addition, wind-stress divergence imparts mean vorticity to the mixed layer whereas wind-stress curl causes the familiar Ekman suction velocity at the mixed-layer base. The latter was invoked by Kroll (1975) to force inertial oscillations in an inviscid stratified interior which he then examined using ray theory. Rubenstein (1983) used a similar approach but did not decouple the interior from the mixed layer, thus allowing an interaction between the two. Also, using a numerical model, Rubenstein treated all frequency components of the forcing simultaneously rather than specifying a single frequency component. Earlier models by Pollard (1970) and Pollard and Millard (1970) used the same forcing mechanism (wind-stress curl) and examined the inertial oscillations as a function of depth by means of normal mode expansions in the vertical. Krauss (1979) addressed the question of inertial oscillations (horizontal and vertical) in a channel of finite width and depth but infinite in length. Krauss' model was applied first to one homogeneous layer and then to two homogeneous layers of different densities. Two types of forcing were applied in each case; firstly, using a purely divergent wind stress and secondly, using a purely rotational wind stress.

The above-mentioned models differ from each other in their various refinements, in their methods of solution and in their emphasis on the controlling parameters. The basic forcing mechanism, however, is common to all. The inertial currents must be generated by a storm which is bounded horizontally and which therefore has associated winds which vary spatially. This is doubly significant since not only will near-inertial vertical oscillations (Eq. (4)) develop at the pycnocline and mixed-layer interface, thereby constituting an energy source for inertial waves in the pycnocline, but it will also establish a spatial scale defining the horizontal wavenumber k in the dispersion relation for internal waves:

$$w^2 = f^2 + N^2 k^2 / m^2, \tag{5}$$

where N is the Brunt-Väisälä frequency and m the vertical wavenumber. The vertical group velocity associated with Eq. (5) is

$$c_z = -k^2 N^2 / w m^3. \tag{6}$$

It was shown quite rigorously in Kroll (1975) that the forcing frequency at the mixed-layer base will differ from the local value of f by a small positive amount if pressure

– 13 –

terms are included in the Ekman layer equations; in our case Eq. (1). Kroll also points out that the non-linear terms excluded from the same equations may also have a modifying influence on the inertial frequency. It seems reasonable to suppose the same will be true of horizontal diffusion.

Since the forcing frequency w is determined in the surface layer and must be greater than f, and since k is also determined by the spatial scale of the storm, Eq. (5) shows that m is finite and the vertical group velocity (Eq. (6)) is non-zero and positive downward. Near-inertial energy thus propagates downward at small angles to the horizontal and can, in the relatively low levels of turbulent dissipation in and below the pycnocline, propagate over long distances. If this mechanism, one of strong spatial variations in the wind-stress forcing, is in fact operating in or near the MILEX-82 area, one would expect the forcing to take place in the areas of strongest wind-stress curl several hundreds of kilometres to the north. This area is known (May, 1982) to have an exceptionally high wind-stress curl both in monthly and seasonal means due to persistence of the Mistral wind with its narrow jet-like profile. In support, measured values of the Ekman suction velocites have been reported (Voorhis and Webb, 1970) during the MEDOC cruise of up to 2 cm/s. Such events would be accompanied by extremely energetic near-inertial oscillations in the vertical.

A possible explanation for the delayed response of the thermocline to the wind, therefore, might be that the response is not to the local wind but rather to the wind 250 km to the North. The inertial waves would have to be travelling southward with group velocity about 250 km in 18 h. The current meters, however, in contrast to their thermistor chains, do not show this same delayed response to the wind (see Fig. 23 of Sect. 5) and so do not support this distant source hypothesis. On the other hand, as pointed out by Schott (1971), the most energetic waves for the horizontal motions (detectable by current meters) may be separated in the wavenumber spectrum from the most energetic waves for the vertical motions (detectable by thermistor chains); the vertical motions tending to associate with higher wavenumber. In this case one might expect a different group velocity and arrival time for the respective wave trains.

■ *4.3.3. Instability mechanisms*

More recent theories for downward propagating inertial waves involve instability mechanisms due to Kroll (1982) and Kroll (1984). In Kroll (1982) a uniform slab flow of the mixed layer is assumed, in which there are no inertial oscillations. The linearized perturbation equations for the upper slab layer and the lower stratified layer are shown to be unstable for certain combinations of the governing parameters. The length scale of the instability is of the order 10 km and is thus supportive of observations of coherence scales for inertial motions below the mixed layer (Pollard, 1980; Sandford, 1975). An interesting feature of the instability is that it does not depend on spatial variations in wind stress.

- 14 -

The second, related, instability mechanism (Kroll, 1984) is both more realistic (since it includes inertial oscillations in the 'mean' slab-flow) and, as it turns out, more unstable. The linearized perturbation equations are essentially those of Kroll (1982) but with coefficients that include time periodic components (i.e. components representing the inertial currents in the mixed layer). Instability arising in such equations is known as parametric instability and the solutions, especially in this case, are rather complicated. Nevertheless, some interesting results which are relevant to the interpretation of the MILEX-82 data emerge. In a comparison of theory with data Kroll chose parameters observed at site D presented in Pollard (1980). He found that instability was possible for a small region of the parameter space provided the horizontal length scale $L = \sqrt{\nu_H}/f$ was less than about 2.5 km. Here ν_H is a coefficient for horizontal turbulent diffusion in the mixed layer. To ensure a good correspondence with the measured mean flow, however, a rather small choice of L must be made which leads to a horizontal wavelength for the near inertial oscillations as low as 1.2 km. Although this seems unrealistically short for a wavelength, it represents a lower bound, and the estimate in any case appears quite sensitive to the choice of some of the variable parameters. Since there is a reasonable similarity between the Pollard (1980) data, referred to by Kroll, and that of MILEX-82, we might expect the instability to be operating in the MILEX-82 area. To be more precise one would have to make fresh calculations using Kroll's model.

Another set of parameters presented in Kroll (1984), as realistic, and in our case bearing some similarity to MILEX-82 data, gave an e-folding growth time for the most unstable solution of 1.3 days. This growth time could offer an alternative explanation of the delayed thermocline response to the rapid changes in wind stress.

In summary, it is likely that both the spatially varying wind stress and the parametric instability mechanisms could explain the presence of vertical oscillations in the MILEX-82 area. Furthermore, both mechanisms can explain the delayed response of the thermocline to the wind. To determine which is the more likely mechanism critical tests would be required applying, for example, Kroll's (1984) model to the MILEX-82 parameters on the one hand, and then on the other hand applying either the model due to Kroll (1975) or Rubenstein (1982) to the hypothesized generation zone to the North and studying the effect in the MILEX-82 area.

4.4. SUPER-INERTIAL FREQUENCIES

It is quite evident from the isotherm plots of Figs. 15 to 17 that vertical oscillations are also occurring at approximately twice the local inertial frequency. A good example is again the period covering days 280 to 286 in Fig. 15b. By day 282 a very pronounced double peak is occurring on the inertial waves and as time passes the inertial motions attenuate and become confused with the super-inertial motions ($\omega \approx 2f$) which themselves remain detectable until the end of the record (Fig. 15c).

Similar observations of super-inertial motions have been reported by Titov (1973), Krauss (1981) and Pinkel (1983). Although not specifically mentioned, other examples can be found in the temperature variance spectra of, for example, Weller and Halpern (1983) and Moen (1984).

Relative to the inertial waves, these higher frequency components are associated with high downward vertical group velocities (see Eqs. (5) and (6)), thus making them efficient in extracting energy from the mixed-layer flow. This has been pointed out by several investigators, for example Krauss (1981), Rubenstein (1983) and Kroll (1984).

4.5. TEMPERATURE SPECTRA

To better illustrate the presence of super-inertial vertical oscillations, spectra of temperature variance are presented in Figs. 18 to 20 and spectra of isotherm displacement in Fig. 21. In these (particularly in Fig. 21) significant peaks can be seen at roughly integral multiples of the inertial frequency; in some cases up to a factor of four. Rubenstein (1983) has pointed out that such super-inertial components are probably the result of non-linear interaction between near-inertial waves and represent a sink of energy for the inertial motions. In Kroll (1984) super-inertial waves are a prediction of the parametric instability mechanism and can be taken, according to Kroll, as evidence that the mechanism is operating. The frequencies in Kroll's case should occur not at nf but rather at $\omega + nf$, where n is an integer and ω is the near inertial frequency of the unstable oscillations in the mixed-layer flow. Unfortunately, due averaging over five adjacent frequency bands, the resolution of the spectra in Figs. 18 to 20 is not good enough to distinguish between nf and $\omega + nf$ for the super-inertial frequencies. For such a fine distinction the records ought to be re-analysed using complex demodulation.

4.6. PHASE RESOLUTION

Before continuing to discuss current-meter data, it is interesting to examine the isotherm plots for phase changes with depth. In the case of shallow seas, for example, it has been both observed and predicted (Krauss, 1979) that a two-layer structure to the inertial motions will develop with an upper layer 180° out of phase with a lower layer. It is not clear that the same should be true of the vertical oscillations and especially in much deeper water such as in the MILEX-82 area. The clearest example of phase changes that can be seen directly in the isotherm plots is for days 280 to 286 at mooring A. The phase shifts, illustrated in Fig. 22, indicate that the phase does change over some region of the thermocline between 40 and 60 m but the change is not constant in time and does not reach the value 180° (i.e. 9.3 h at this latitude). The upper and lower levels of the thermocline appear to be in

phase at the onset of the vertical oscillations on day 280. Curiously, the upper level then begins to lag the lower, first by a few hours, and reaching a maximum of 7 h by day 285. Although the vertical group velocity is downward, therefore, as defined by Eq. (6), Fig. 22 indicates an upward directed vertical phase speed ($C_p = \omega/m$) consistent with observations by Pollard (1980). Whether or not the phase changes of Fig. 22 are typical of all the thermistor chain data is difficult to tell without further analysis such as complex demodulation mentioned earlier.

Of particular interest in Fig. 25 are phase angles between the 40 and 60 m depths and the 60 and 80 m depths, since these three current meters were on the same mooring, until day 295 when the mixed-layer deepened to beyond 40 m (Fig. 31), they were situated well within the pycnocline. On day 270 the 40 and 60 m inertial currents were in phase, but by day 275 they were out of phase by about 245°, where they remained for about 4 to 5 days. They came back into phase by day 282.5, then went about 180° out again during the period spanning days 285 to 287.5, back into phase by day 290, 90° out by day 295.5 and finally remaining within 45° for the last 10 days. The recordings for 6ᴼ and 80 m remain closer in phase apart from a brief period around day 287.5 when they became almost 180° out of phase. These periods of antiphase between closely spaced current meters would tend to raise the level of turbulent diffusion through shear production. The levels of shear, together with buoyancy frequency and Richardson number are presented in Sect. 6.

In other examples of phase variations which can be followed in Fig. 25 it would not be possible, due to horizontal separation of current meters, to attribute phase differences only to vertical dispersion. Nevertheless, the high variability in phase over such small separations is surprising and suggests that coherence between records estimated over the entire measuring period would be low. Although it will not be presented here, a more thorough treatment would require estimating phase as a function of time by, for example, the method of complex demodulation (Perkins, 1970; Pollard and Tarbell, 1975). This would, in addition, provide information on the small shifts in frequency from the local inertial value.

5.3. FREQUENCY DISPERSION

The variations in phase described above (Sect. 5.2) might be due in part to a variation in frequency of the near-inertial motions with depth. Although complex demodulation was not performed on the MILEX-82 data, some idea of the variations in near inertial frequency can be extracted from the stick plots of Fig. 23. The records for each current meter were divided into 5-day intervals and the mean inertial period for each interval was estimated by measuring the time required for 5, 6 or 7 complete oscillations. Cases that were not clear, or that contained sudden phase changes were not included. End points were determined by requiring end vectors to be aligned, if necessary, by an approximate interpolation between adjacent vectors. Results of this analysis are presented in Table 1 as a percentage above the local inertial frequency $(f = 2\pi/18.66 \ h^{-1})$.

We see that frequency is indeed dispersed in some way both with depth and time – the extremes ranging from −2% to +15%. Of particular interest are the differences between the 40 and 60 m depths demonstrated earlier to be variously in and out of phase. It would appear from this somewhat crude analysis that the frequency at 40 m is decreasing with time from about $1.15f$ on day 275 to about f by day 300. At

- 20 -

Table 1
Mean inertial periods for selected 5-day intervals

Depth (m)	Time interval (Julian days)							Mean inertial period
	270/ 275	275/ 280	280/ 285	285/ 290	290/ 295	295/ 300	300/ 305	
10	0	0	2					0.7
20	0	− 1	2					0.3
30	7	4	4	0				4.3
40	10	15	4	4	2	0	1	5.1
60	5	5	7	5	15	2		6.5
80	5	− 1	5	7	0	4	2	3.1
120	2	2	13	8	− 2			4.6
160		4	4	4	8	15	4	6.5

60 m, on the other hand, the frequency increases over the same period from about $1.05f$ to $1.15f$. Looking at the mean values, there is a tendency for the frequency to increase with depth, or at least for the mixed-layer oscillations to be significantly lower in freqeuncy ($< 1.01f$) than those of the pycnocline ($1.05f$).

This sort of dispersion can be explained by the dispersion relation (Eq. 4.5) and vertical group velocity expression (Eq. 4.6) for inertial-internal waves. As pointed out by several authors (e.g. Kroll, 1975; Krauss, 1979; Rubenstein, 1983) sudden temporal changes in wind speed can excite a spectrum of near-inertial waves in the upper ocean, and for a fixed stratification N those wave packets with lowest vertical wavenumber m will have the highest frequency ω . Also, these same wave packets will have the highest downward group velocities, causing the higher-frequency inertial energy to disappear first from the upper-most layer. Of course the mixed layer is not stratified and so for finite values of k^2/m^2, where k is the horizontal wavenumber, Eq. (4.5) shows that the frequency will tend towards f.

There are other dynamics-related reasons why the inertial frequency just below the mixed layer will be greater than f. These were discussed in Sect. 4.3 in connection with the vertical oscillations. It was pointed out that the oscillations can only enter the pycnocline below the mixed layer through either an Ekman suction mechanism (Kroll, 1975) or through instability mechanisms of the mixed-layer flow (Kroll, 1983; Kroll, 1984). It was also argued that if the deeper oscillations were due to the former mechanisms they were probably not generated locally, but rather to the north in regions of high spatial variations in wind stress. Support for the instability mechanisms for the generation of sub-mixed-layer oscillations comes with the observation of energy peaks in the velocity spectra (Fig. 26) at higher harmonics of the in-

ertial frequency (Kroll, 1984). These were also observed in the temperature and isotherm spectra presented in Sect. 4.5. Although such super-inertial oscillations are a prediction of Kroll's instability theory, inertial oscillations are, in any case, weakly non-linear and so as pointed out by Rubenstein (1984), a non-linear term like $u\, \partial v/\partial x$ can easily reach 10% of linear terms in the momentum balance. The effect of non-linearities is to generate higher harmonics of the inertial frequency. Another strong non-linearity, of course, occurs in the transition zone between mixed layer and pycnocline. Here one can compare the x-momentum balance term $w\, \partial u/\partial z$ with fv, assuming the pycnocline to be initally quiescent; if not, the inertial motions can be out of phase with the mixed layer as is often the case (Krauss, 1979; also recall the phase lag between 20 and 30 m noted earlier in Sect. 5.2) causing even higher values of the shear $\partial u/\partial z$. Estimates of the shear in the 20 to 30 m layer (see Fig. 27 of Sect. 6) show sustained values of $0.05\ s^{-1}$. For the same period (days 280 to 285), the isotherm plots of Fig. 15 show a crest-to-trough range near the interface of 4 m/inertial cycle, which converts to a vertical velocity amplitude of 0.02 cm/s. Taking a v-velocity of 15 cm/s, which is about the amplitude deduced by linear interpolation between 20 and 30 m or between 30 and 40 m (Fig. 23), gives a value of $1.5 \times 10^{-3}\ cm/s^2$ for fv compared to $1.0 \times 10^{-3}\ cm/s^2$ for $w\, \partial u/\partial z$. Non-linear terms, therefore, are of the same order as linear terms and it is hardly surprising that super-inertial oscillations are observed.

The discussion to this point has been on near-inertial frequencies, including higher harmonics, which occur below the mixed layer. It is important to note that the essentially horizontal oscillations which characterize the mixed layer can also differ by small amounts in frequency from the local value of f. There appear to be three main reasons why this is so. The first reason has to do with the effect of small pressure gradient forces (Kroll, 1975) usually neglected in boundary layer analysis of inertial waves. Kroll showed analytically how pressure effects in the linearized boundary layer equations can cause a slight increase in the inertial frequency and then he assumed the result to hold in the non-linear case. On the basis of Kroll's analysis, and as mentioned earlier in Sect. 4.3, one might assume further that other effects, also normally neglected, such as linear and non-linear advection and horizontal diffusion, would also cause small changes in the inertial frequency.

The second reason for observed changes in the inertial frequency could be due to a doppler shift. Schott (1971) has pointed out that for inertial waves with a 50 km wavelength such as he observed in the northern North Sea, a 1% frequency variation near the inertial frequency only needs a mean current of 1 cm/s along the propagation path of the wave.

Finally, the third reason involves spatial variations in the underlying quasi-geostrophic flow field (Fomin, 1973; Weller, 1982). Contributions by other authors to this topic are reviewed in Weller's paper. In simple terms, water particles in the mixed layer accelerated by changes in wind stress attempt to move in straight lines confined to the earth's surface by gravity. However, since the 'background' is rotating both

– 22 –

due to earth rotation and pre-existing vorticity, the particles will appear to travel in elliptical orbits. The frequency of these motions will, therefore, differ from f, the local inertial frequency fixed by latitude, according to the sign and strength of the background vorticity.

With reference to the dynamic anomaly plots of Fig. 11 and the stick diagrams of Fig. 23, both the doppler and vorticity effects on f ought to be minimal in the MILEX-82 region. This might explain the relatively small deviations to f presented in the mixed layer portion of Table 1.

5.4. VELOCITY SPECTRA

Rotary spectra for the upper 6 current meters are presented in the composite plot of Fig. 26. Those for the NBA current meters at 120 m and 160 m have been omitted since there is evidence that these were severly 'pumped' by mooring line oscillations in the vertical as discussed earlier in Sect. 2.2. The method of averaging over adjacent frequency bands, as a method of increasing confidence in the spectra, has decreased resolution to the extent that small deviations from f in the local inertial frequency cannot be resolved.

The spectra of Fig. 26 confirm the predominance observed earlier in the stick plots (Fig. 23) of the highly clockwise rotational inertial oscillations. Not only is there a peak at the inertial frequency but clockwise energy appears to saturate a large band of super-inertial frequencies down to about 4 h periods. Within this band, as with the temperature variance spectra of Figs. 18 to 20, smaller peaks can be observed at higher harmonics of the near-inertial frequency. In the mixed-layer spectra (10 and 20 m) these peaks must be due to non-linear effects discussed above (Sect. 5.3), whereas in the deeper layers (particularly 60 and 80 m), where arguably the clockwise band has relatively more energy, they could be due to both non-linearity and parametric instability mechanisms (Kroll, 1982 and 1984) discussed in Sects. 4.3 and 5.3. The anticlockwise spectrum at 40 m shows quite pronounced peaks at the inertial and double inertial frequencies, implying that the motion is more elliptic at 40 m than for the other depths.

6. Other parameters

This section contains time series plots of various measured or estimated parameters which are directly relevant to mixed-layer deepening and which will be of interest in any comparison of the data with mixed-layer models for the MILEX-82 area.

Three sets of parameters are presented. In the first set, bulk values of shear S, Brunt-Väisälä frequency N, and Richardson number Ri were calculated according to the formulae

$$S^2 = \frac{(u_1 - u_2)^2 + (v_1 - v_2)^2}{(z_1 - z_2)^2},$$

$$N^2 = -g\alpha \frac{(T_1 - T_2)}{(z_1 - z_2)},$$

$$\mathrm{Ri} = N^2/S^2, \tag{7}$$

where the subscripts 1 and 2 refer to the upper and lower current meter levels respectively, the temperatures T_1 and T_2 were estimated by linear interpolation on the thermistor chain data, and α is the coefficient of thermal expansion for sea water. Errors in expression (Eq. (7)) occur due to neglecting effects of horizontal separation of current meters, neglecting differences in velocity due to type of current meter and in neglecting salinity effects on density. The latter error is of the order 10% in the MILEX-82 area. Plots of S, N and Ri are displayed in Figs. 27 to 30. Values for the intervals 80 to 120 m and 120 to 160 m are not shown since the two NBA current meters (at 120 and 160 m), as discussed earlier, produced unreliable results.

The second set of parameters (Fig. 31a,d) are: mixed-layer depth, maximum Brunt-Väisälä frequency, change in heat content and change in potential energy. To calculate these, cubic spline functions were fitted to the thermistor chain data and then, using the appropriate analytic formula for each spline section, the depth of minimum second derivative, $\partial^2 T/\partial z^2$ was defined as the mixed-layer depth, the maximum first derivative, $\partial T/\partial z$ was used to calculate N, and the integrals

$$\Delta H(t) = \rho C_p \int_{-D}^{0} (T(t) - T(0)) \, dz,$$

$$\Delta PE(t) = -g\rho\alpha \int_{-D}^{0} (T(t) - T(0)) z \, dz \tag{8}$$

were evaluated to give the heat content and potential energy respectively. In Eq. (8) C_p is the specific heat for sea water, α the coefficient of thermal expansion and D the

depth of the thermistor chain at mooring B. The error in potential energy change due to neglecting salinity effects on density is estimated to be less than 10%.

Finally, the third set of parameters (Fig. 32a,d) comprise plots cf barometric pressure BP, wind speed WS, air temperature AT, sea-surface temperature ST and estimates of sensible and latent heat fluxes QS and QL respectively. The derivation of QS and QL involved first estimating QS from a bulk aerodynamic formula and then, estimating QL using an empirical formula for the Bowen ratio, $B = QS/QL$, dependent on air/sea temperature difference and wind speed. Further details of the method are presented in Moen (1984). Both the second and third set of parameters (Figs. 31 and 32) derive from instruments at mooring B since these presented the longest time series.

We can now make a number of comments regarding the parameters plotted. The Richardson number Ri shown in Figs. 27 to 30 measures dynamic stability in the presence of stratification and is thus an indication of mixing. As defined by Eq. (7), Ri is a bulk value over a 10 m or, in some cases, a 20 m layer, so that according to Pollard et al. (1973) mixing will occur if its value drops below unity – the mechanism being one of high levels of production of turbulent mixing energy, attributable not only to the mean shear but also to breaking internal waves.

Scanning the plots (Figs. 27 to 30) we see that with few exceptions Ri remains below 1 both within the mixed layer, as expected, and across the mixed layer base during the entire period of measurements. There are also periods of potential mixing showing up in the thermocline. For example, for the layer 40–60 m, Ri is less than 1 more or less continuously during days 285–287 and periodically (with inertial frequency) during days 290–294 and 297–300. Similarly, for the 60–80 m layer Ri falls below 1 on three occasions between days 285 and 287 and for about 30% of the time during days 2970–301. Reference back to Fig. 25 shows that, at least for the period days 285–287, the 40 m and 60 m current vectors are 180° out of phase. Vertical variations in phase of the inertial oscillations, therefore, can have a significant effect on mixing within the thermocline.

It is perhaps a point of curiosity that with the bulk gradient Richardson number being so frequently below unity across the mixed-layer/thermocline interface, more deepening of the mixed layer diū not occur.

The expression for changes in potential energy given by Eq. (8) assumes no horizontal or vertical advection is taking place. The expression is equivalent, to the lowest order in $\alpha\Delta T$, to the more accurate and physically meaningful method of calculating potential energy where vertical integration begins at a geopotential surface and continues up to the free surface, thereby allowing for expansion of the water column. Since a downwelling, such as occurs during half of an inertial cycle, will cause the measured portion of the water column to be warmer, Eq. (8) will yield, incorrectly, an increase in potential energy. That is, an expansion of the water column (through

– 25 –

heating) is assumed to have taken place. Inertial cycles in the potential energy plots of Fig. 31, therefore, are meaningless as would be any other advective effects on potential energy estimates by Eq. (8).

A possible advective effect might explain why for the period days 294–296 the heat content and potential energy both increase (Fig. 31) despite the mixed layer having deepened from 36 to 44 m and the air temperature having dropped from 22 to 19 °C (Fig. 32). By day 300, however, the heat content has dropped to its day–294 value but the potential energy remains high, reflecting the mixing that has occurred. Another example of mixing increasing the potential energy can be seen for the period, days 280–285 (Fig. 31). Here the mixed layer deepens from 32 to 38 m but the maximum buoyancy and heat content show only slight changes, whereas the potential energy increases quite noticeably.

Returning to the heating of the water mentioned above for days 294–296 (Fig. 31c), it should be pointed out that despite the strong cooling by latent and sensible heat losses (Fig. 32c) there might have been a net radiative heating for the same period. There is no direct evidence for this since cloud cover statistics were not taken, but one can imagine the colder and perhaps drier air to have been associated with cloud-free skies. Radiative heating, therefore, presents an alternative speculation to advective effects for the observed increase in heat content and consequent increase in potential energy for the two-day period.

7. Summary and conclusions

In this section, points of summary, conclusion or recommendation are presented in an order approximately following their discussion in the report.

7.1. SPATIAL DESCRIPTION

(1) Two hydrographic surveys were conducted: one during mooring deployment ($\sim$ 43 CTD stations and 180 XBT casts) and one by the Italian Navy during late October ($\sim$ 16 CTD stations and 120 XBT casts. These data form the basis of the spatial descriptions.

(2) In describing the spatial structure a distinction was made between an upper or 'surface' layer of about 150 m depth and a deeper 'intermediate' layer from about 150 to 1000 m. This division was somewhat arbitrary and although corresponding to about the lower portion of the seasonal thermocline it has no special dynamical significance. Rather, it had to do with display; the very strong vertical gradients of the surface layer required large contour intervals, and these would have been masked if the layers had not been viewed separately; the relatively weaker structure is present in the intermediate layer.

(3) The upper layer showed an essentially uniform spatial structure in the study zone with no large-scale variations in the south-north direction. However, shallowing of the potentially mixed layer was seen in both the temperature and salinity west-east sections on approaching the Sardinian shelf break. Since the surface temperature was also warmer in this region, the shallowing of the layer (probably caused by upwelling) must have been happening slowly compared with the heating time-scale through insolation.

(4) The general pattern of geostrophic flow through the study area relative to motion at 1000 m appeared consistent with the maps presented in Ovchinnikov (1966). In the upper 200 m the eastward flowing North African current branched northward into a portion of the study area and then flowed southeastward again causing an anticyclonic motion which appeared to have almost pinched off, into an eddy. At the 20 m level a partially-formed cyclonic gyre was identified in the northeast portion of the study area. This was associated with the cold, possibly upwelled, water showing up in the temperature data referred to in the preceding paragraph (item 3). The geostrophic flow near the mooring sites was southward at about 7 cm/s.

(5) The deeper layer (150 to 1000 m) was characterized by the so-called 'Levantine Water' lying approximately between 300 and 650 m. This water, showing general agreement with transects presented in the Mediterranean Atlas of

Miller, Tchernia and Charnock (1970), indicated a weak north-south gradient in temperature and salinity – both decreasing to the south.

The most striking features of the deeper layer were the warm and cold temperature 'blobs', density – compensated by their salinity, which were observed just above the Levantine Water. Within the Levantine Water of the western portion of the study area several of the CTD profiles indicated a fairly pronounced step-like structure.

7.2. TEMPORAL DESCRIPTION (THERMISTOR-CHAIN DATA)

(1) Time series for the approximately 40-day period were collected from 3 moored thermistor chains, each chain consisting of 22 thermistors spanning mixed layer and thermocline (to $\sim$ 100 m depth) and separated one chain from the other by about 10 km, in a triangular arrangement.

(2) Periodic vertical displacement of isotherms indicated inertial or near-inertial frequency motion to have been present throughout the measurement period. Indeed, these motions dominated the records – particularly, as expected, after the onset of the storm events.

(3) The amplitude of the oscillations was frequently seen to be greater in the more weakly stratified water below the thermocline than in the thermocline itself. The total energy of the vertical oscillations, however, may not have been increasing with depth in the same way, since the buoyancy restoring forces due to stratification were a higher in the upper than in the lower thermocline.

(4) A significant delay between onset of vertical oscillations and sudden increase in wind speed (in one case $\sim$ 24 h) was noted on several occasions. This observation was brought to bear on the possible generation mechanism for the vertical oscillations. Four possible mechanisms were discussed:

(i) Advection of sloping isopycnal surfaces by horizontal inertial oscillations.

(ii) A horizontal Ekman mass-flux divergence due to a spatially varying wind stress. The inertial frequency component of this diverging mass flux then forces complementary vertical oscillations (Kroll, 1975).

(iii) A parametric instability (Kroll, 1982 and 1984) of a slab-like mixed-layer flow (inertially oscillating or not) when subjected suddenly to a spatially uniform wind stress.

(iv) Vertical inertial oscillations generated elsewhere, particularly by mechanism (ii) above, may also have propagated into the study area.

Of these mechanisms, (iii) and (iv) were the only ones to offer explanation of the apparently delayed response of the vertical inertial oscillations to the

sudden strong changes in the wind stress, such as occurred several times during MILEX-82.

(5) A fifth mechanism capable of generating vertical inertial oscillations locally might arise from step changes in a spatially uniform wind stress over water with a high background vorticity. This might occur, for example, when a storm passes over a geostrophic eddy. Such a mechanism was not discussed in the text of the report and was unlikely to have been relevant to the study area; no eddies were observed either by satellite or from the hydrographic data during MILEX-82. Details of the potential mechanism do not appear in the literature but they can be deduced (not to be presented here) from the Ekman-layer/geostrophic-layer modelling presented in Stern (1975).

(6) Vertical oscillations super-inertial in frequency ($\omega = 2f$) were also observed in the records. As has been pointed out, for example by Krauss (1981), Rubenstein (1983) and Kroll (1984), these higher-frequency components are associated with high downward vertical group velocities and are thus efficient in extracting energy from the mixed-layer flow. This would explain why the mixed layer did not deepen more, considering the severity of the storm events during MILEX-82. That is to say mixing energy may have been propagating out of the mixed layer, leaving reduced amounts available for mixing.

According to Kroll (1984) super-inertial waves are a prediction of the parametric instability mechanism (item 4 (iii) above) for generation of vertical inertial oscillations. Their presence, therefore, is suportive (although not exclusively so) of the instability mechanism.

(7) The vertical near-inertial oscillations did not display a constant phase with depth and the phase shifts were not constant with time. Although a 180° phase shift is predicted and observed (Krauss, 1979) in a two-layer shallow water model for the horizontal oscillations, it is not clear why phase changes with depth should be taking place in the case of deep stratified water. Further and more detailed analyses of these data using techniques such as complex demodulations are recommended.

7.3. TEMPORAL DESCRIPTION (CURRENT-METER DATA)

(1) Vertical arrays of current meters, distributed between the three mooring locations, together provided flow information for the upper (150 m) layer.

(2) The mean flows are relatively weak (in the 1 to 10 cm/s range) at all depths, but the inertial oscillations were of quite high amplitude (up to 50 cm/s), particularly in the surface mixed-layer after sudden large increases in wind stress.

(3) The mixed-layer flow was 'slab-like', but with the inertial oscillations at the layer base ($\sim$ 30 m) mostly out of phase with the layer itself by about 90° ± 40°.

(4) Unlike the vertical, the horizontal oscillations responded rapidly to the sudden changes in wind stress of day 279. This was seen in the mixed layer as not an amplitude response but a sudden phase change of the existing inertial oscillations.

(5) The amplitude response was found to be slower, with a delay of about 14 h. Two reasons for this are possible: firstly, before they could grow in amplitude the new oscillations had to overcome or cancel the existing out-of-phase oscillations; and secondly, there was a marked tendency for the wind vector to rotate in a counter-clockwise sense, thus opposing the very inertial motions it was generating.

(6) An interesting feature of the inertial currents was in the variability of their phase with both depth and time. Sustained periods of large phase differences and even periods of antiphase occurred within the thermocline, particularly in the 40 to 60 m depth range. The resulting, relatively large shear caused lower values of the Richardson number in this region, creating the conditions for a raised level of turbulent diffusion.

(7) The variability in phase was itself seen to be largely a manifestation of changes in the near-inertial frequency with depth and time. In the mean, there was a tendency for frequency to increase with depth – the mixed-layer value of about $1.01f$ being less than the pycnocline value of about $1.05f$. Over a 25-day period the frequency at 40 m was to decrease from $1.15f$ to $1.0f$ while at 60 m it increased during the same period from $1.05f$ to $1.15f$.

(8) The observed value of the near-inertial frequency in the mixed layer can only differ significantly from the local value of f if there is a high background geostrophic vorticity ω present in the water column. The relatively small deviation of the near-inertial from the inertial frequency observed in the mixed layer of the MILEX-82 study area was therefore testimony to the very low background or geosptrophic vorticity present there.

(9) Reasons for the variability in near-inertial frequencies were presented as:

(i) the tendency for higher frequency inertial energy to have faster down-

ward group velocity, causing it to disappear from the mixed layer more quickly; and

(ii) deeper inertial-energy may have been generated well north of the study area (as mentioned for the vertical oscillations – Sects. 4.3 and 7.2) where the local value of f was much higher.

(10) Super-inertial frequency motions were seen as secondary peaks in the velocity spectra. These were most likely a result of strong non-linearity due to interaction between the vertical and horizontal inertial oscillations (i.e. terms in the momentum balance such as $w \, \partial u/\partial z$). Estimates from the data showed this term in the mixed-layer/thermocline interface region to be of a similar order effect, to the Coriolis term (fv) itself.

7.4. OTHER PARAMETERS

(1) Time-series plots were presented for the following measured or derived parameters: vertical current shear, Brunt-Väisälä frequency, bulk gradient Richardson number, mixed-layer depth, maximum Brunt-Väisälä frequency, change in water column heat content, change in water-column potential energy, barometric pressure, wind speed, air temperature, sea-surface temperature and finally estimated sensible and latent heat fluxes.

(2) The estimated gradient Richardson numbers for 2 levels within the thermocline were found to be below unity during a number of prolonged periods. These periods coresponded to times of large vertical changes in the phase of the inertial oscillations, confirming the importance of inertial-wave phase variations with depth to mixing within the thermocline.

References

CREPON, M., WALD, L. and MONGET, J.M. Low-frequency waves in the Ligurian Sea during December 1977. *Journal of Geophysical Research*, **87**, 1982: 595–600.

FOMIN, L.M. Inertial oscillations in a horizontally inhomogeneous current velocity field in the ocean. *Izvestiya Atmospheric and Oceanic Physics*, **9**, 1973: 75–83.

KLEIN, P. A simulation of the effects of air-sea transfer variability on the structure of marine upper layers. *Journal of Physical Oceanography*, **10**, 1980: 1824–1841.

KRAUSS, W. Inertial waves in an infinite channel of rectangular cross section. *Deutsche Hydrographische Zeitschrift*, **32**, 1979: 248–266.

KRAUSS, W. The erosion of a thermocline. *Journal of Physical Oceanography*, **11**, 1981: 415–433.

KROLL, J. The propagation of wind-generated inertial oscillations from the surface into the deep ocean. *Journal of Marine Research*, **33**, 1975: 15–51.

KROLL, J. An unstable uniform slab model of the mixed layer as a source of downward propagating near-inertial motion. Part 1: Steady mean flow. *Journal of Marine Research*, **40**, 1982: 1013–1033.

KROLL, J. An unstable uniform slab model of the mixed layer as a source of downward propagating near-inertial motion. Part 2: Unsteady mean flow. *Journal of Marine Research*, **42**, 1984: 83–102.

MAY, P.W. Climatological flux estimates in the Mediterranean Sea: Part 1: Winds and wind stresses, NORDA REPORT 54. NSTL Station MS, Naval Ocean Research and Development Activity, 1382. [AD A 121 931].

MILLER, A.R., TCHERNIA, P. and CHARNOCK, H. Mediterranean Sea Atlas of temperature, salinity oxygen profiles and data from cruises of R.V. *Atlantis* and R.V. *Chain*. Woods Hole, MA, Woods Hole Oceanographic Institution, 1970.

MOEN, J. Variability and mixing of the surface layer in the Tyrrhenian Sea: MILEX-80, final Report. SACLANTCEN SR-75, La Spezia, Italy, SACLANT ASW Research Centre, 1984. [AD A 141 929]

OVCHINNIKOV, I.M. Circulation in the surface and intermediate layers of the Mediterranean Sea, *Oceanology*, **6**, 1966: 48–59.

PERKINS, H.T. Inertial oscillations in the Mediterranean. Ph.D. thesis, ISSPP., Woods Hole Massachusetts, MA, Woods Hole Oceanographic Institution, 1970.

PINKEL, R. Doppler sonar observations of internal waves: wave-field structure. *Journal of Physical Oceanography*, **132**, 1983: 804–815.

POLLARD, R.T. On the generation by winds of inertial waves in the ocean. *Deep-Sea Research*, **17**, 1970: 795–812.

POLLARD, R.T. and MILLARD, Jr., R.C. Comparison between observed and simulated wind-generated inertial oscillations. *Deep-Sea Research*, **17**, 1970: 813–821.

POLLARD, R.T., RHINES, P.B. and THOMPSON, R.O.R.Y. The deepening of the wind-mixed layer. *Geophysical Fluid Dynamics*, **3**, 1973: 381–404.

POLLARD, R.T. and TARBELL, S. A compilation of moored current meter and wind observations, Vol. VIII (1970 array experiment). WHOI Ref. 75-7 (unpublished manuscript). Woods Hole, MA, Woods Hole Oceanographic Institution, 1975.

POLLARD, R.T. Properties of near-surface inertial oscillations. *Journal of Physical Oceanography*, **10**, 1980: 385–398.

RUBENSTEIN, P.M. Vertical dispersion of inertial waves in the upper ocean. *Journal of Geophysical Research*, **88**, 1983: 4368–4380.

SANDFORD, T.B. Observations of the vertical structure of internal waves. *Journal of Geophysical Research*, **80**, 1975: 3861–3871.

SCHOTT, F. Spatial structure of inertial period motions in a two-layered sea, based on observations. *Journal of Marine Research*, **29**, 1971: 85–102.

STERN, M.E. Ocean circulation physics. New York, NY, Academic Press, 1975.

TITOV, V.B. Some distinctive features of mesoscale motions in the sea. *Oceanology*, **13**, 1973: 794–798.

VOORHIS, A.D. and WEBB, D.C. Large vertical currents observed in a winter sinking region of the northwestern mediterranean. *Cahiers Océanographiques*, **22**, 1970: 571–580.

WEBSTER, F. Observations of inertial-period motions in the deep sea. *Reviews of Geophysics*, **6**, 1968: 473–490.

WELLER, R.A. and DAVIS, R.E. A vector measuring current meter. *Deep-Sea Research*, **27A**, 1980: 565–568.

WELLER, R.A. The relation of near-inertial motions observed in the mixed layer during the JASIN (1978) Experiment to the local wind stress and to the quasi-geostrophic flow field. *Journal of Physical Oceanography*, **12**, 1982: 1122–1136.

WELLER, R.A. and HALPERN, D. The velocity structure of the upper ocean in the presence of surface forcing and mesoscale oceanic eddies. *In*: CHARNOCK, H. and POLLARD, R.T. *eds*. Results of the Royal Society Joint Air-Sea Interaction Project (JASIN). London, The Royal Society, 1983: 327–340.
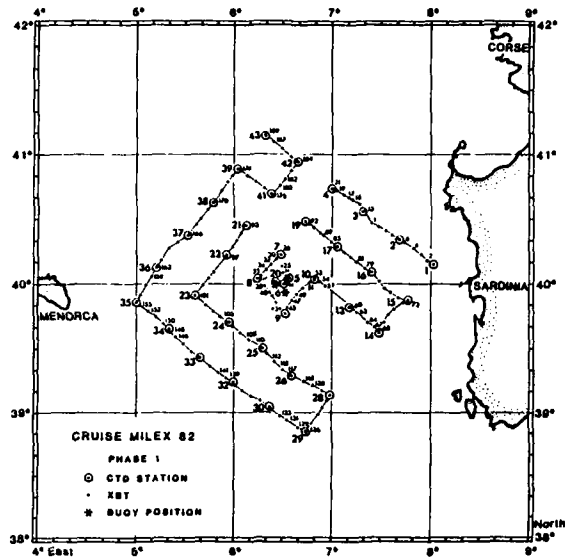
Fig. 1a. Location of MILEX-82 CTD stations (large numbers) and XBT stations (small numbers).
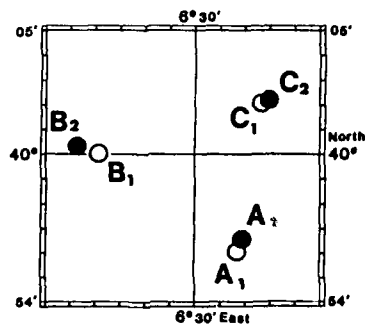
A_1 :   thermistor chain; currentmeter

B_1-C_1 :   thermistor chain; currentmeter; meteo-chain

A_2-B_2-C_2 :   currentmeter

Fig. 1b. Location of MILEX-82 moorings.
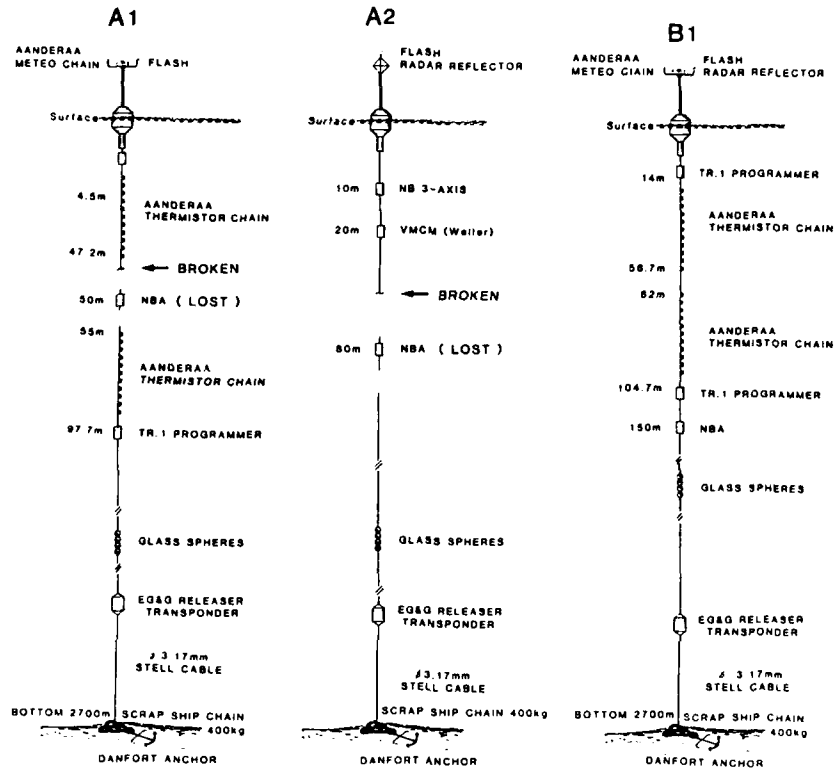
Fig. 2. Schematic representation of the six moorings.

B2

FLASH
RADAR REFLECTOR

Surface

40m   VACM

60m   VACM

80m   NB 3-AXIS

GLASS SPHERES

EG&G RELEASER
TRANSPONDER

ø 3 17mm
STEEL CABLE

SCRAP SHIP CHAIN
400kg

DANFORTH ANCHOR

C1

FLASH
RADAR REFLECTOR

Surface

15m   TR.1 PROGRAMMER

AANDERAA
THERMISTOR CHAIN

57.7m
63m

AANDERAA
THERMISTOR CHAIN

105 7m

TR.1 PROGRAMMER

120m   NBA

GLASS SPHERES

EG&G RELEASER
TRANSPOMDER

ø 2 17mm
STEEL CABLE

SCRAP SHIP CHAIN 400kg

DANFORTH ANCHOR

C2

FLASH
RADAR REFLECTOR

Surface

30m   VACM

BROKEN

70m   NBA (LOST)

90m   NBA

GLASS SPHERES

EG&G RELEASER
TRANSPON ER

ø 3 7mm
STEEL CABLE

SCRAP SHIP CHAIN 40 Jkg

DANFORT ANCHOR

Fig. 3. Time-table for MILEX-82 showing sampling interval and depth of deployment for each of the moored instruments. See text further explanation.
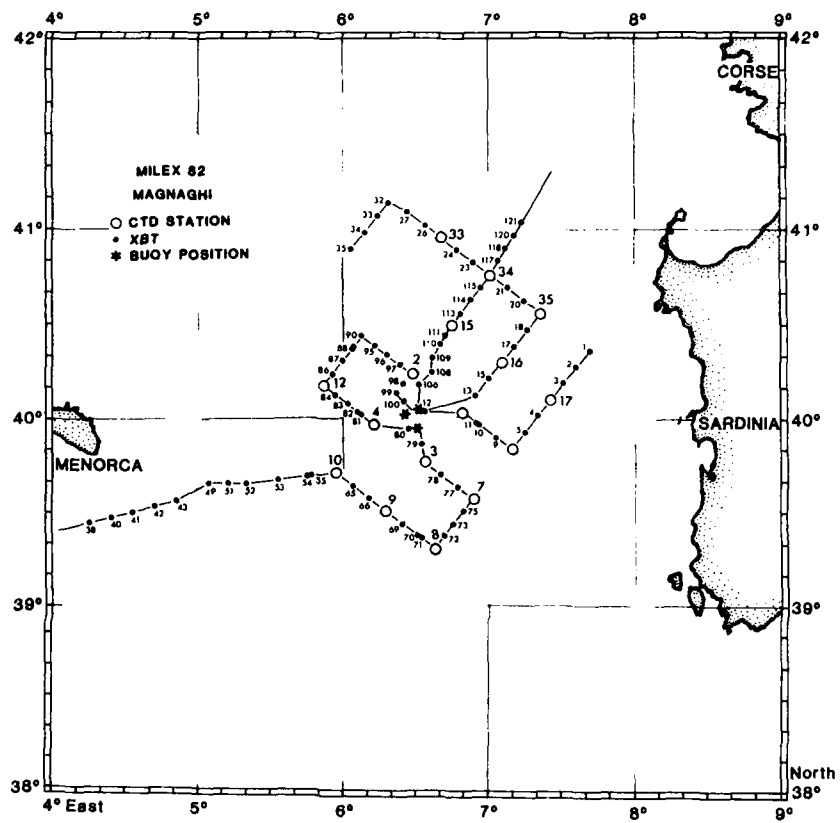
Fig. 4a. CTD/XBT survey track of the Italian Navy hydrographic vessel Ammiraglio Magnaghi.
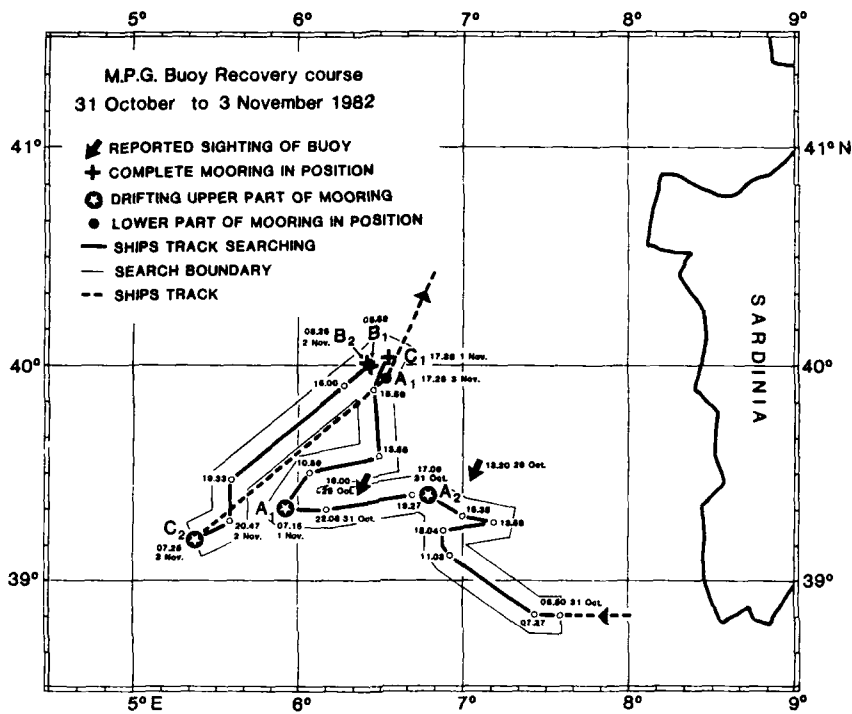
Fig. 4b. Ship's track (*Maria Paolina G.*) for search and recovery of drifting moorings.
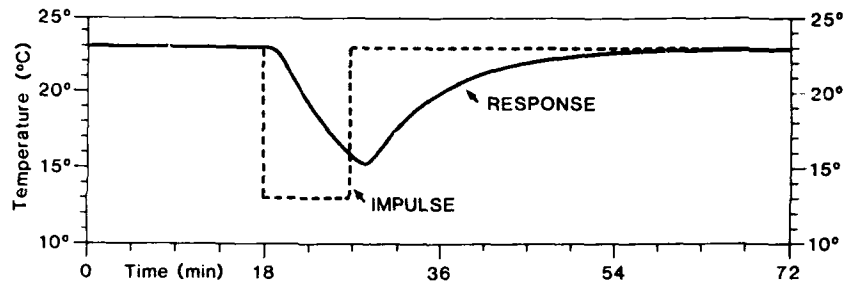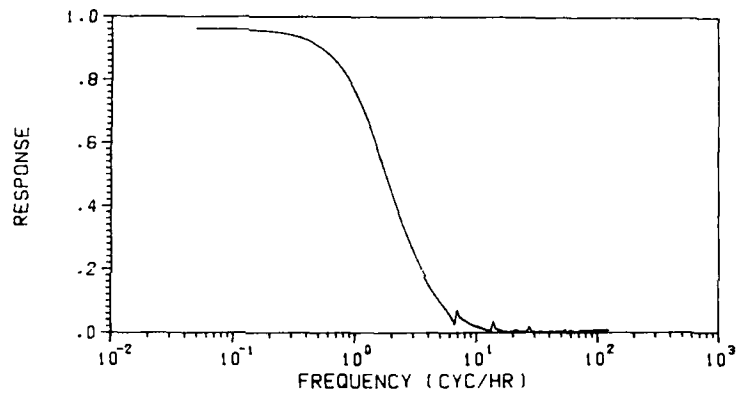
F. RESPONSE FNC.

Fig. 5. Plots of impulse, response and frequency response for the wrapped thermistor.

SOUTH   TEMPERATURE (°C)   NORTH
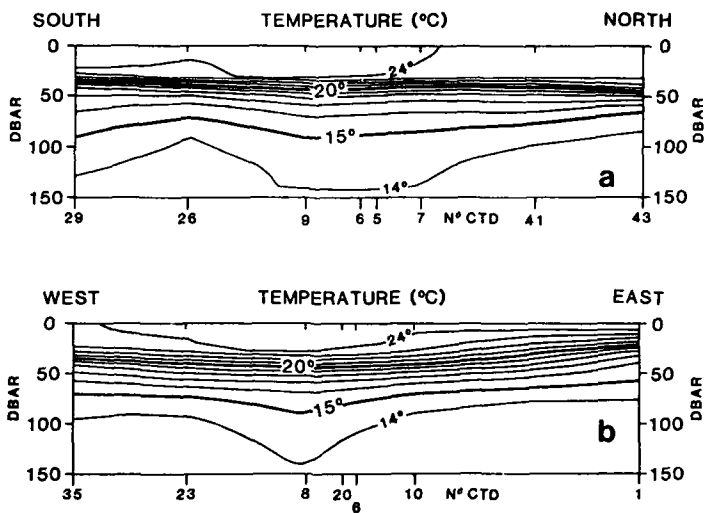
Fig. 6. Vertical temperature sections for the upper 150 m: (a) south-north and (b) west-east.

WEST   TEMPERATURE (°C)   EAST

SOUTH   SALINITY (‰)   NORTH

WEST   SALINITY (‰)   EAST
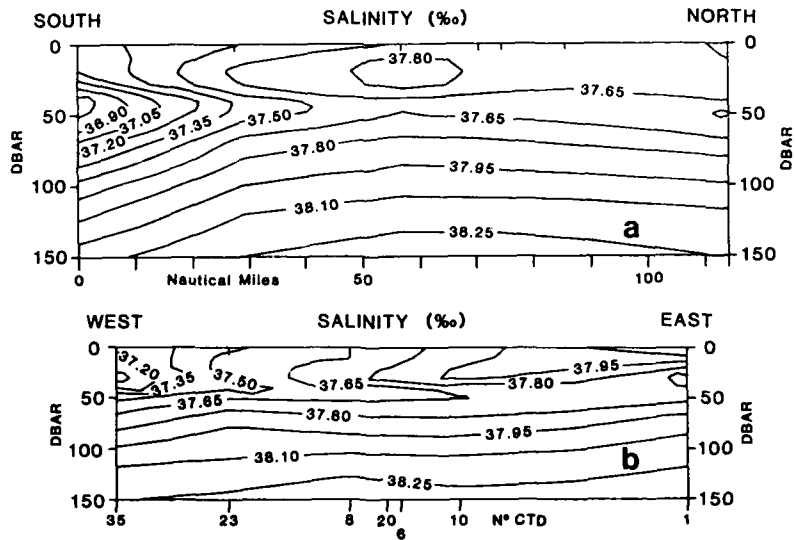
Fig. 7. Vertical salinity sections for the upper 150 m: (a) south-north and (b) west-east.

- @8 -
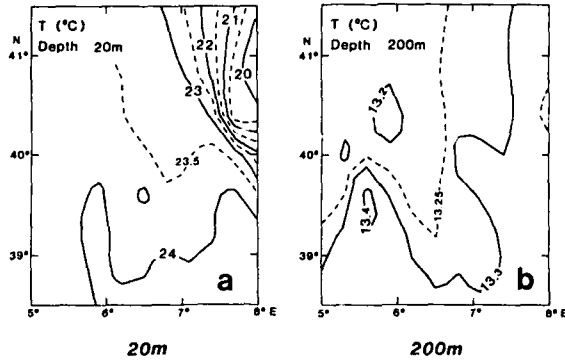
Fig. 8. Horizontal sections of temperature at (a) 20 m and (b) 200 m.
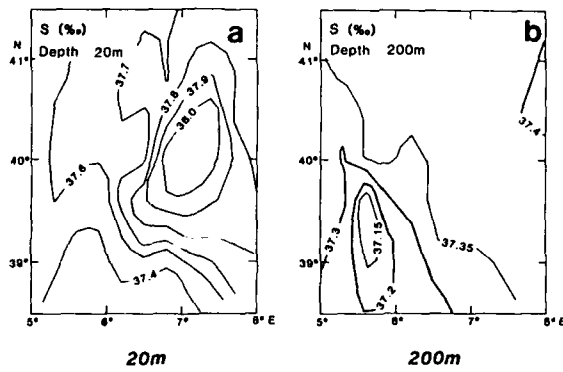
Fig. 9. Horizontal sections of salinity at (a) 20 m and (b) 200 m.
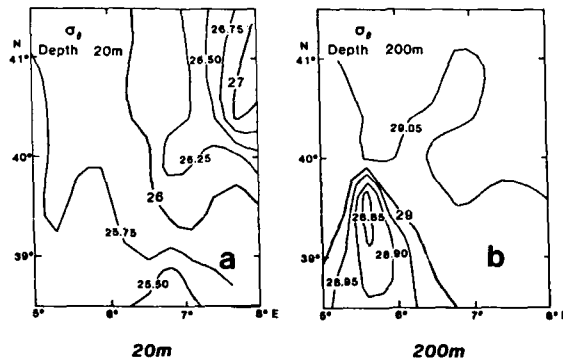
Fig. 10. Horizontal sections of potential density at (a) 20 m and (b) 200 m.

- @9 -

(a)

(b)

20m

200m

(c)

SURFACE
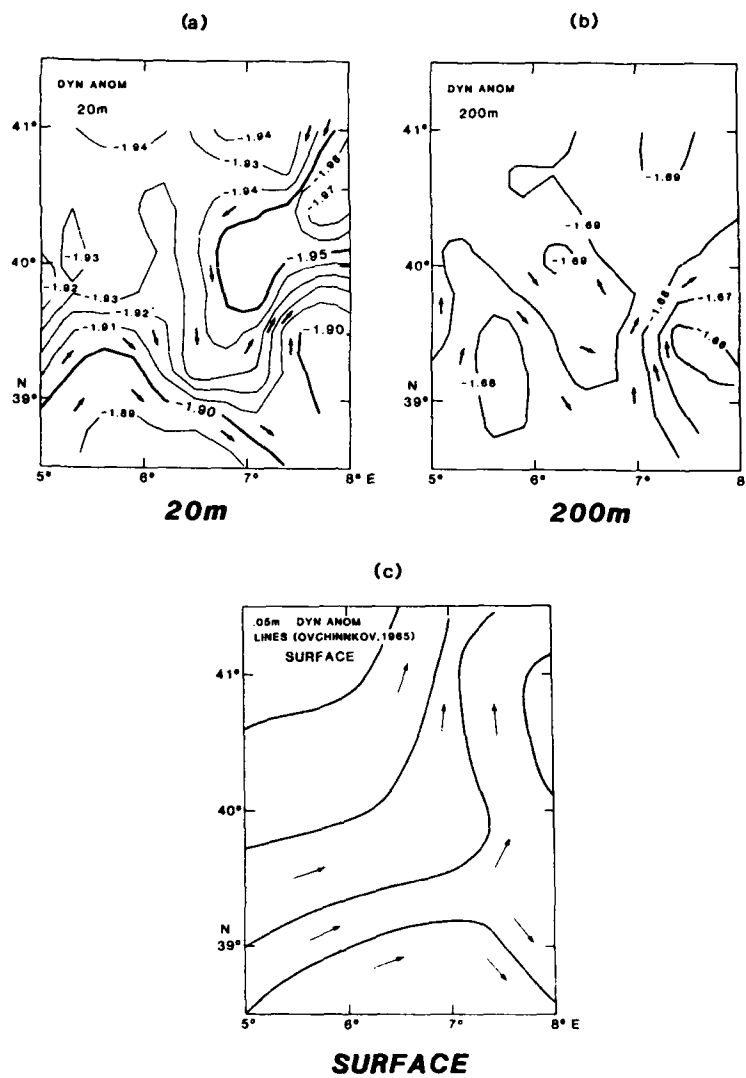
Fig. 11. Dynamic anomaly contours at (a) 20 m. (b) 200 m and (c) reproduced from Ovchinnikov (1965).

SOUTH   TEMPERATURE (C°)   NORTH

WEST   TEMPERATURE (°C)   EAST
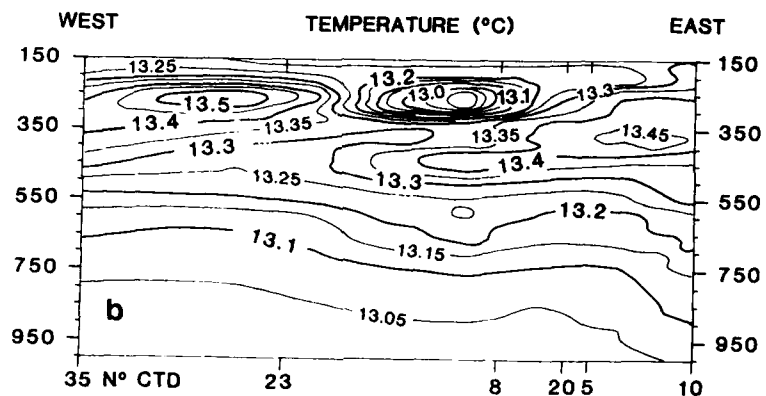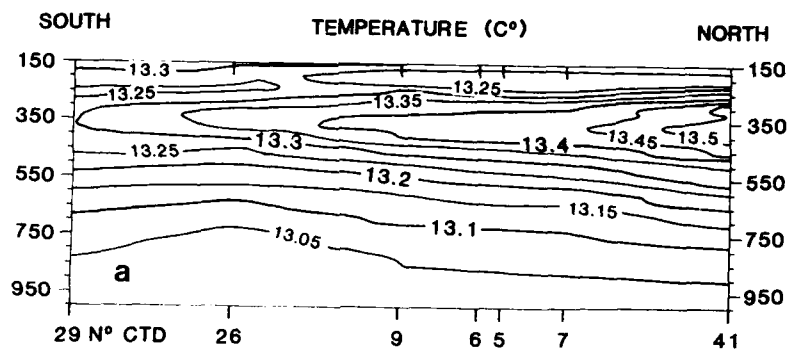
Fig. 12. Vertical temperature sections for the intermediate 150–1000 m layer: (a) south-north and (b) west-east.
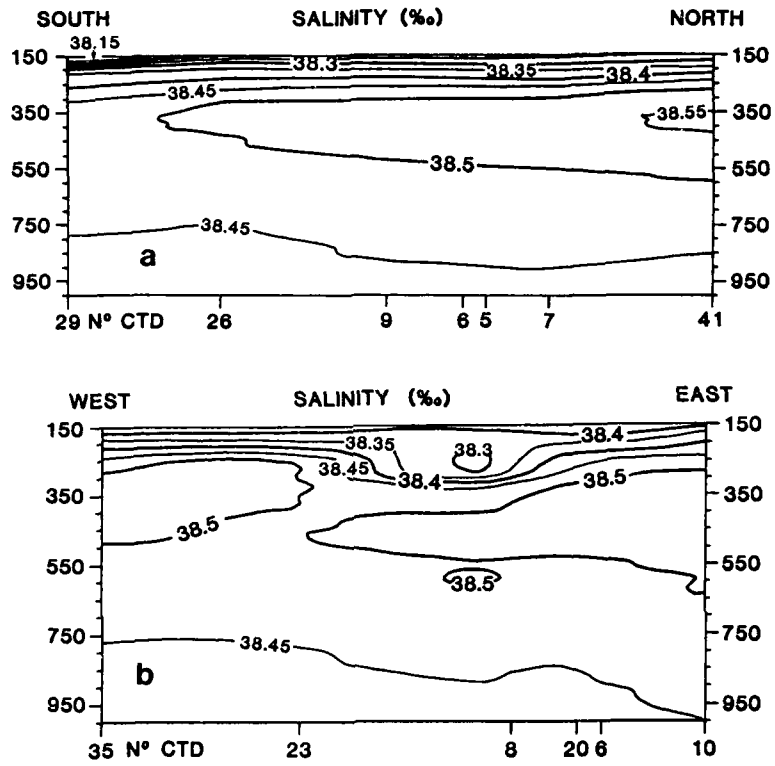
Fig. 13. Vertical salinity sections for the intermediate 150–1000 m layer: (a) south-north and (b) west-east.
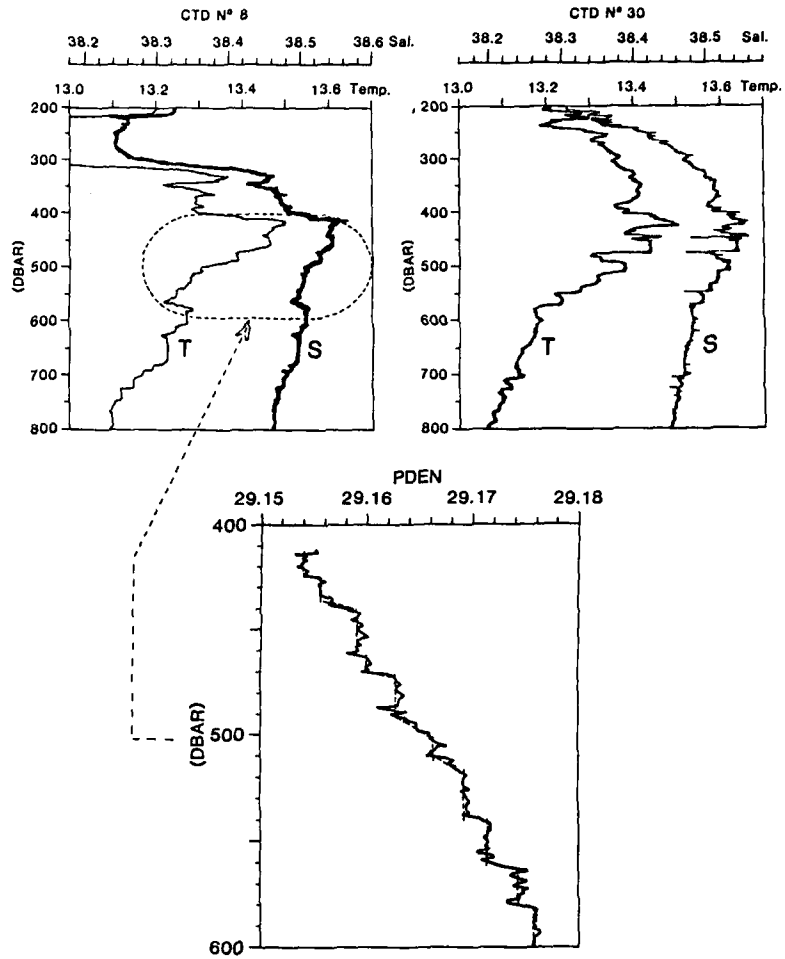
Fig. 14. Example of step-like structure in the Levantine layer observed for CTD stations 8 and 30. The enlargement of steps shown in potential density are for station 8.

MILEX 82 TCA1 (.5 DEG ISOTHERMS)
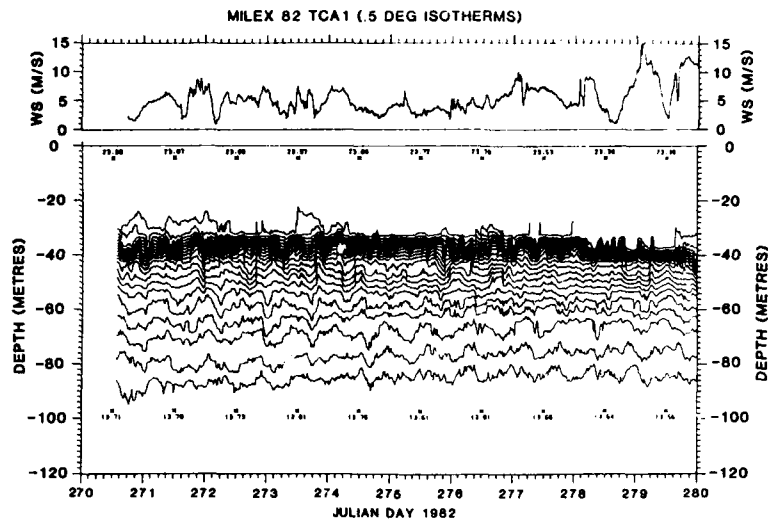
Fig. 15a. Temperature contours from thermistor chain A1 for days 270-280. Contour intervals are every 0.5 °C and positions with temperatures of uppermost-and lowermost thermistors are indicated by a star symbol every 24 h. Wind speed is plotted to indicate wind forcing on the thermocline.

MILEX 82 TCA1 (.5 DEG ISOTHERMS)
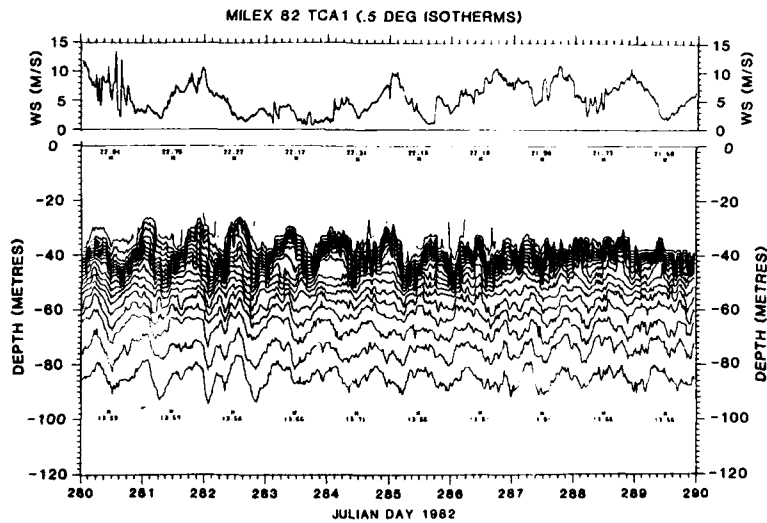
Fig. 15b. Temperature contours from thermistor chain A1 for days 280-290. Contour interval are every 0.5 °C and positions with temperatures of uppermost-and lowermost thermistors are indicated by a star symbol every 24 h. Wind speed is plotted to indicate wind forcing on the thermocline.

– ©14 –

MILEX 82 TCA1 (.5 DEG ISOTHERMS)
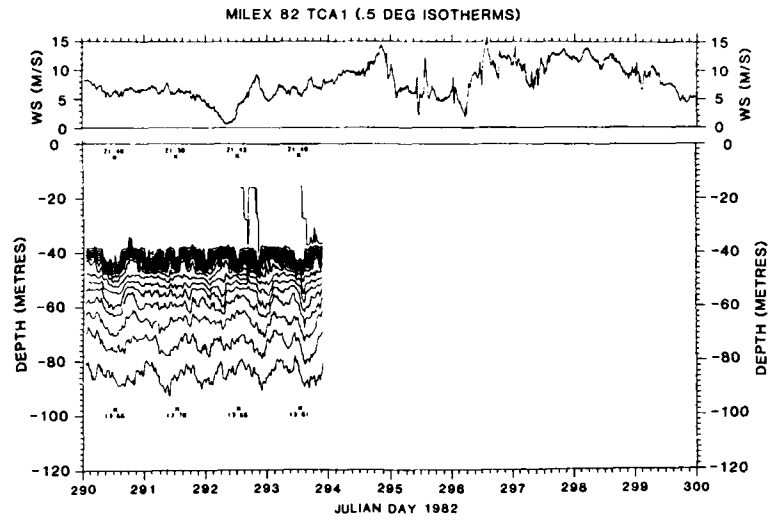
Fig. 15c. Temperature contours from thermistor chain A1 for days 290–300. Contour intervals are very 0.5 °C and positions with temperatures of uppermost-and lowermost thermistors are indicated by a star symbol every 24 h. Wind speed is plotted to indicate wind forcing on the thermocline.

MILEX 82 TCB1 (.5 DEG ISOTHERMS)
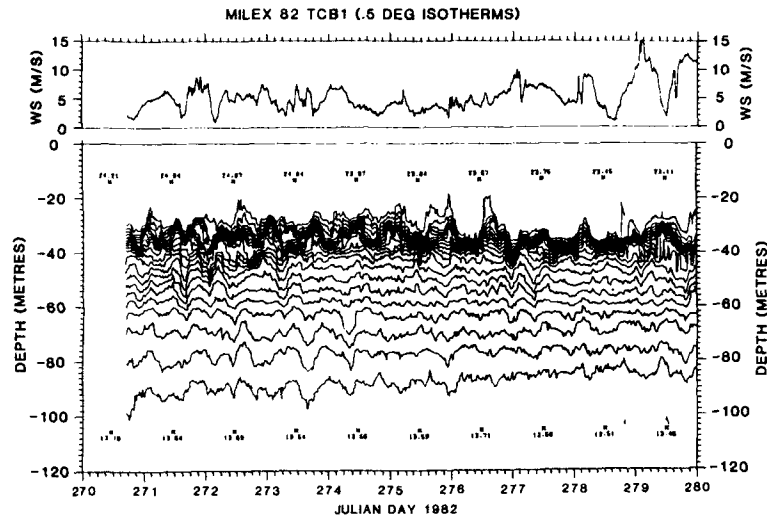
Fig. 16a. Temperature contours from thermistor chain B1 for days 270–280. Contour intervals are every 0.5 °C and positions with temperatures of uppermost-and lowermost thermistors are indicated by a star symbol every 24 h. Wind speed is plotted to indicate wind forcing on the thermocline.

MILEX 82 TCB1 (.5 DEG ISOTHERMS)
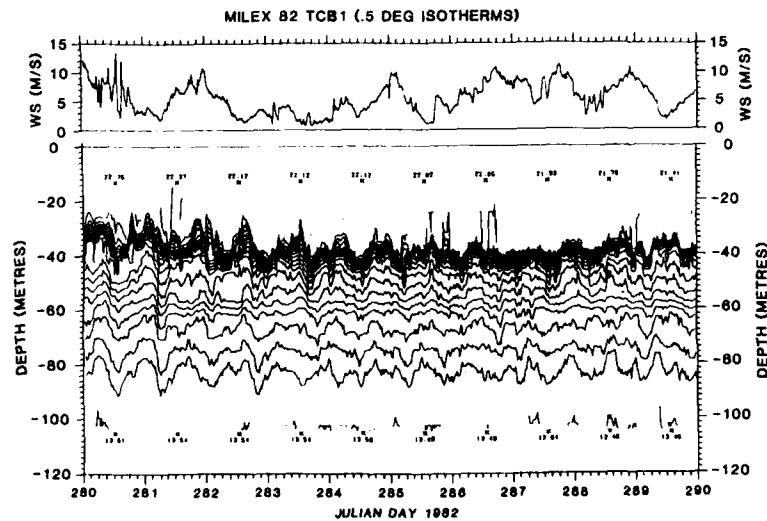
Fig. 16b. Temperature contours from thermistor chain B1 for days 280–290. Contour intervals are every 0.5 °C and positions with temperatures of uppermost-and lowermost thermistors are indicated by a star symbol every 24 h. Wind speed is plotted to indicate wind forcing on the thermocline.

MILEX 82 TCB1 (.5 DEG ISOTHERMS)
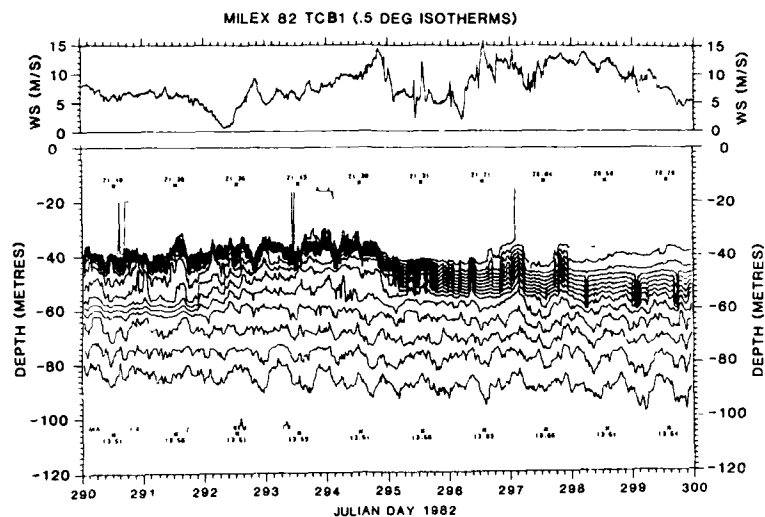
Fig. 16c. Temperature contours from thermistor chain B1 for days 290–300. Contour intervals are every 0.5 °C and positions with temperatures of uppermost-and lowermost thermistors are indicated by a star symbol every 24 h. Wind speed is plotted to indicate wind forcing on the thermocline.

MILEX 82 TCB1 (.5 DEG ISOTHERMS)
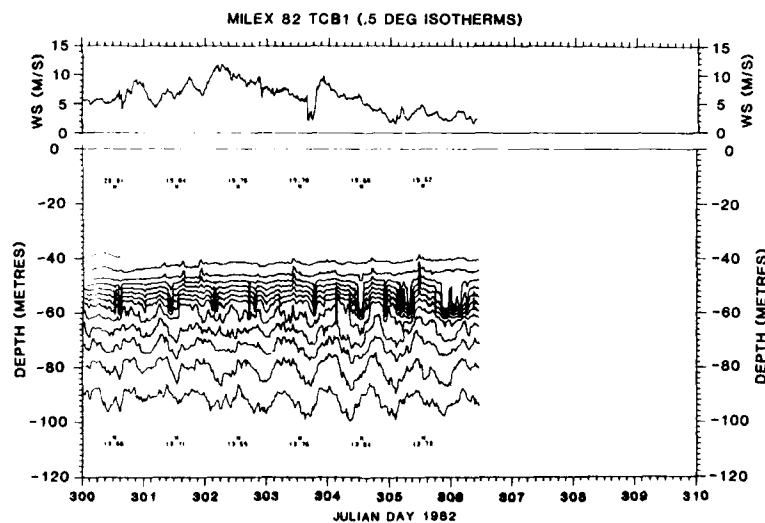
Fig. 16d. Temperature contours from thermistor chain B1 for days 300–310. Contour intervals are every 0.5 °C and positions with temperatures of uppermost-and lowermost thermistors are indicated by a star symbol every 24 h. Wind speed is plotted to indicate wind forcing on the thermocline.

MILEX 82 TCC1 (.5 DEG ISOTHERMS)
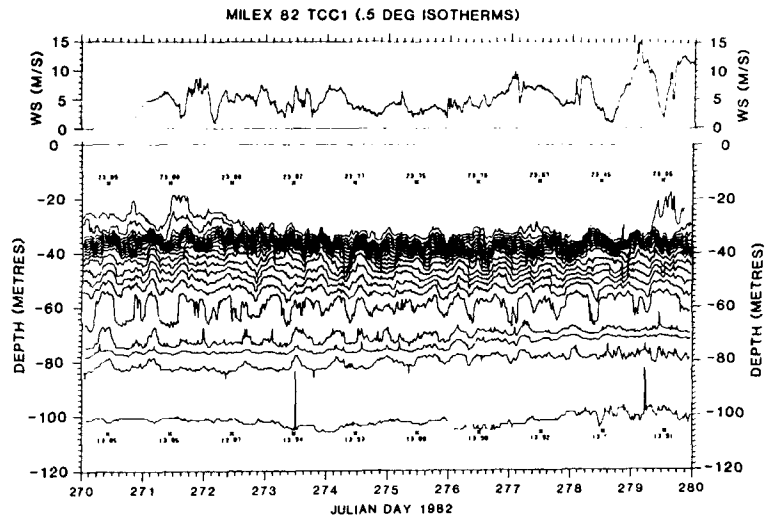
Fig. 17a. Temperature contours from thermistor chain C1 for days 270-280. Contour intervals are every 0.5 °C and positions with temperatures for uppermost-and lowermost thermistors are indicated with a star symbol every 24 h. Wind speed is plotted to indicate wind forcing on the thermocline.

MILEX 82 TCC1 (.5 DEG ISOTHERMS)
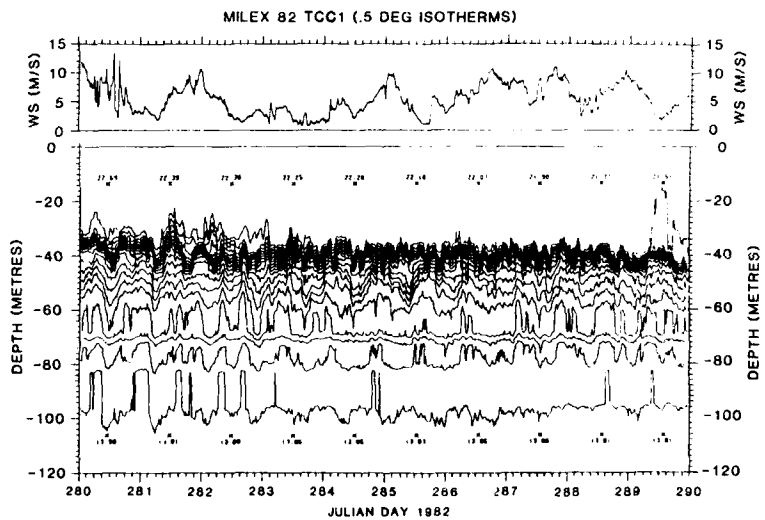
Fig. 17b. Temperature contours from thermistor chain C1 for days 280-290. Contour intervals are very 0.5 °C and positions with temperatures for uppermost-and lowermost thermistors are indicated with a star symbol every 24 h. Wind speed is plotted to indicate wind forcing on the thermocline.

MILEX 82 TCC1 (.5 DEG ISOTHERMS)
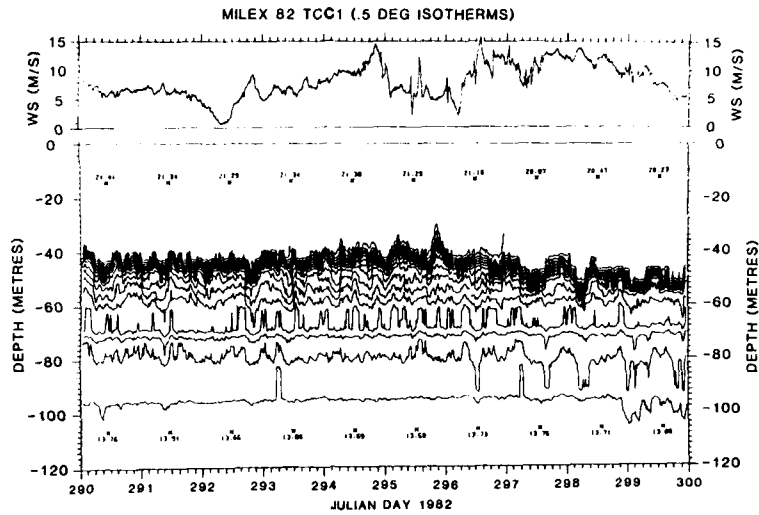
Fig. 17c. Temperature contours from thermistor chain C1 for days 290–300. Contour intervals are every 0.5 °C and positions with temperature for uppermost-and lowermost thermistors are indicated with a star symbol every 24 h. Wind speed is plotted to indicate wind frequency on the thermocline.

MILEX 82 TCC1 (.5 DEG ISOTHERMS)
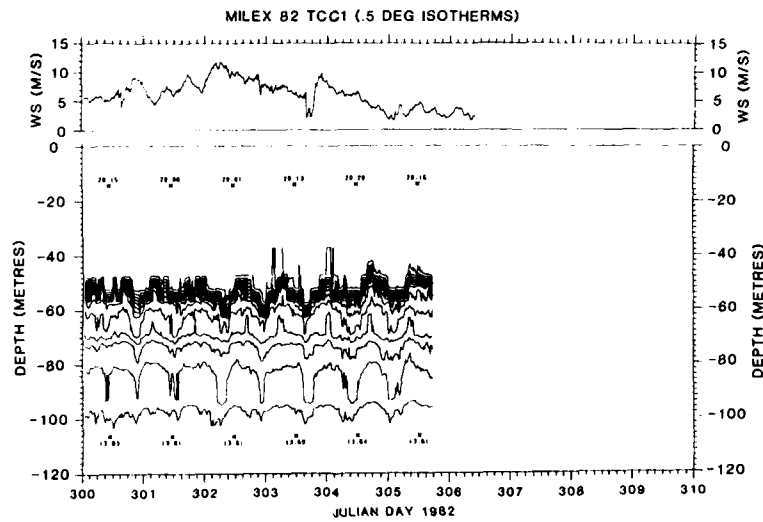
Fig. 17d. Temperature contours from thermistor chain C1 for days 300–310. Contour intervals are every 0.5 °C and positions with temperatures for uppermost-and lowermost thermistors are indicated with a star symbol every 24 h. Wind speed is plotted to indicate wind forcing on the thermocline.
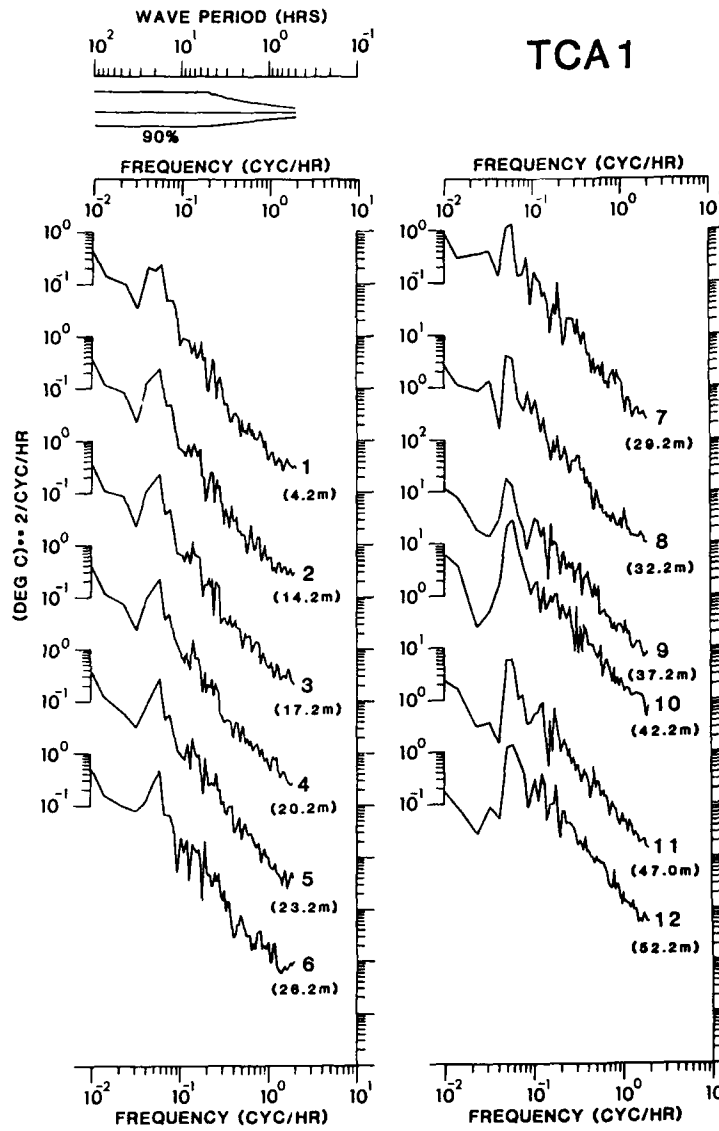
Fig. 18a. Temperature variance spectra for the upper 12 thermistors at mooring A1.

Fig. 18b. Temperature variance spectra for the lower 10 thermistors and the chain average at mooring A1.
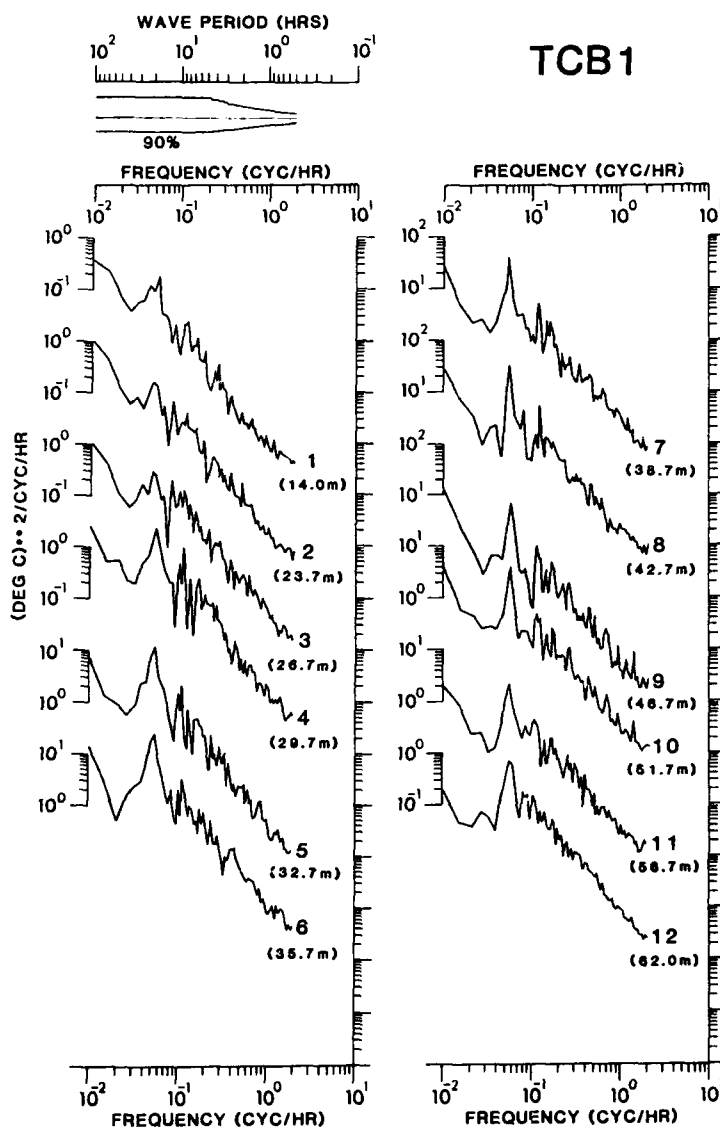
Fig. 19a. Temperature variance spectra for the upper 12 thermistors at mooring B1.
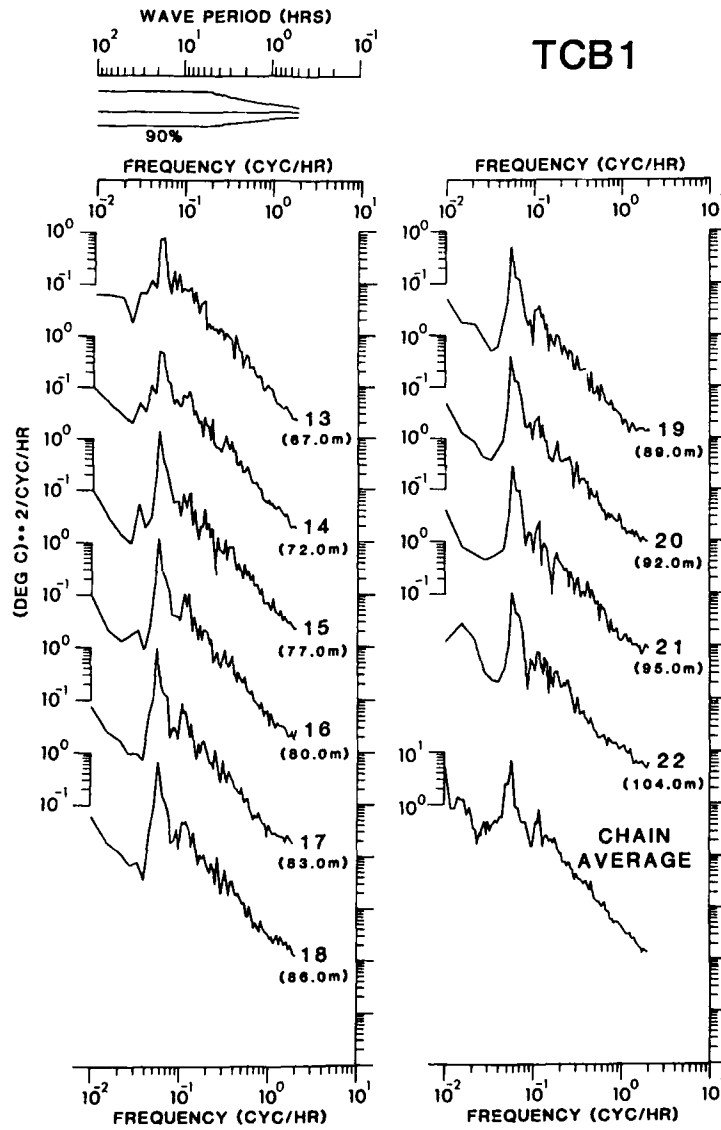
Fig. 19b. Temperature variance spectra for the lower 10 thermistors and the chain average at mooring B1.
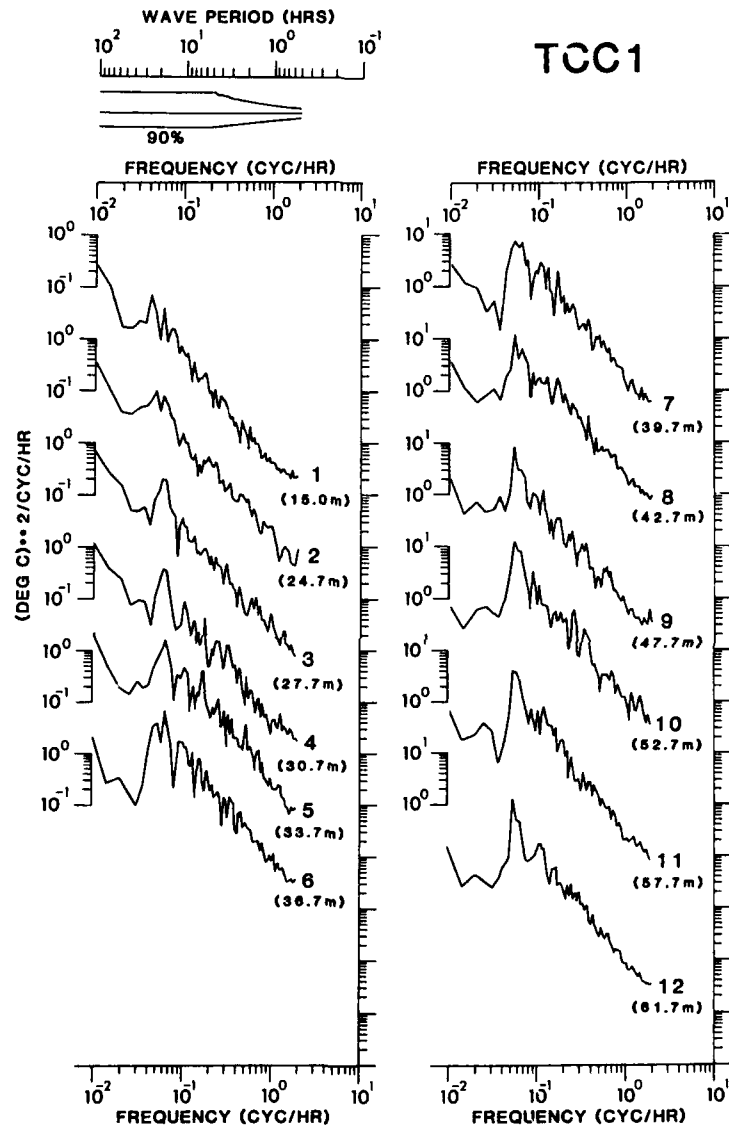
Fig. 20a. Temperature variance spectra for the upper 12 thermistors at mooring C1.
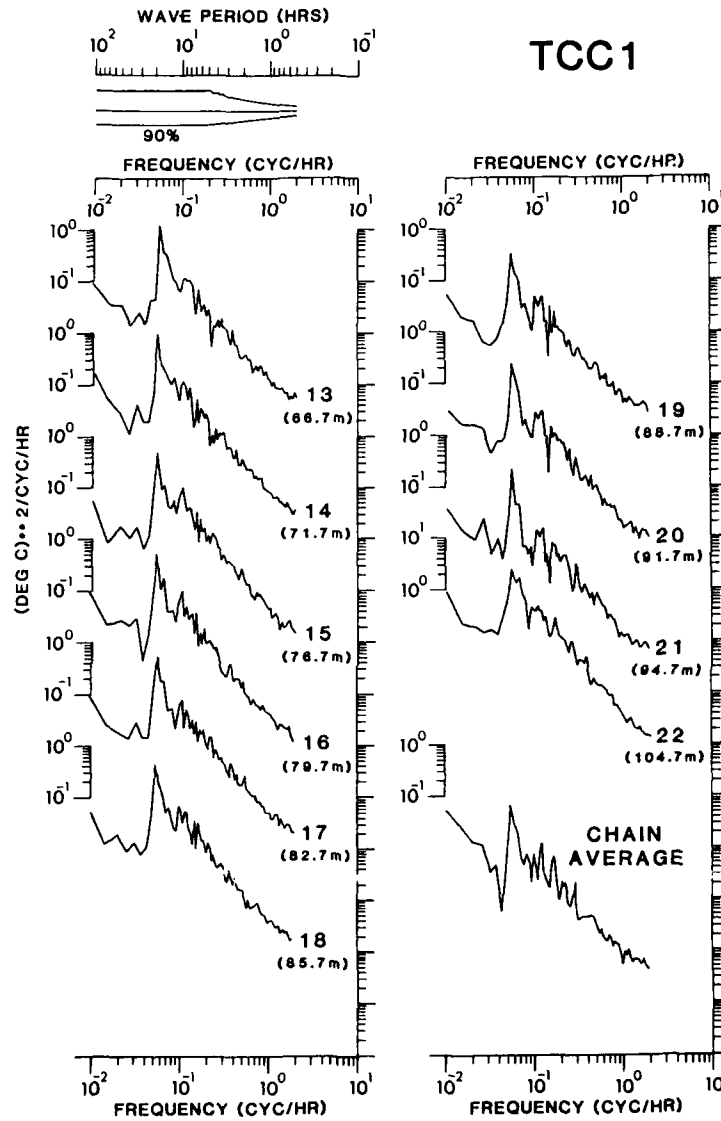
Fig. 20b. Temperature variance for the lower 10 thermistors and chain average of mooring C1.
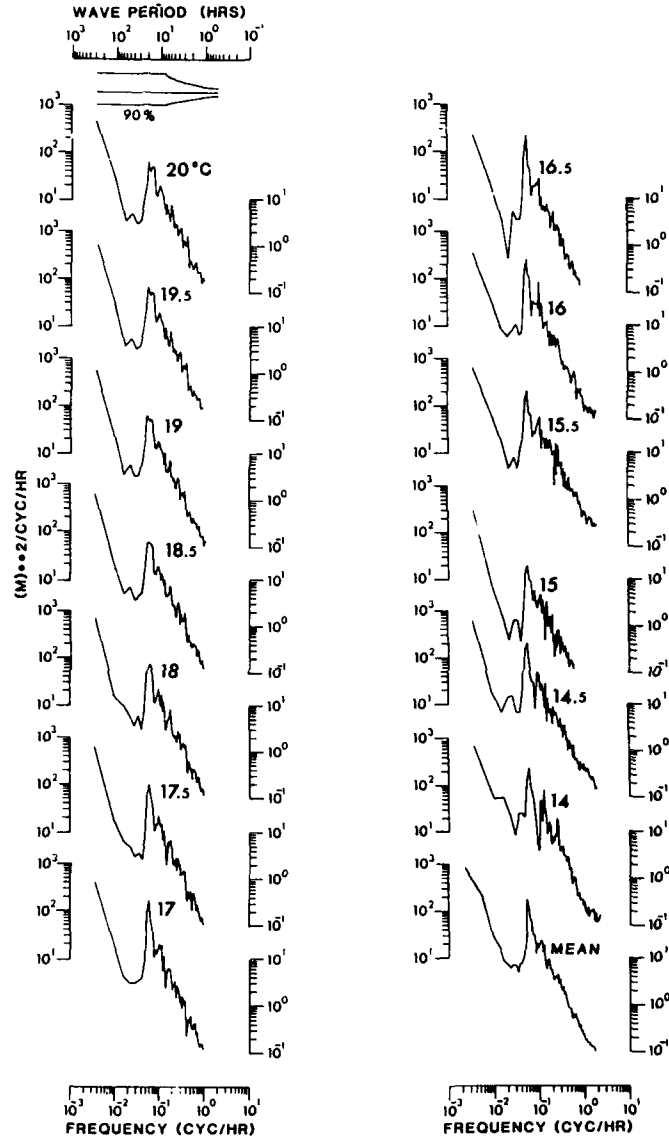
Fig. 21. Spectra for isotherm displacement at mooring C1.
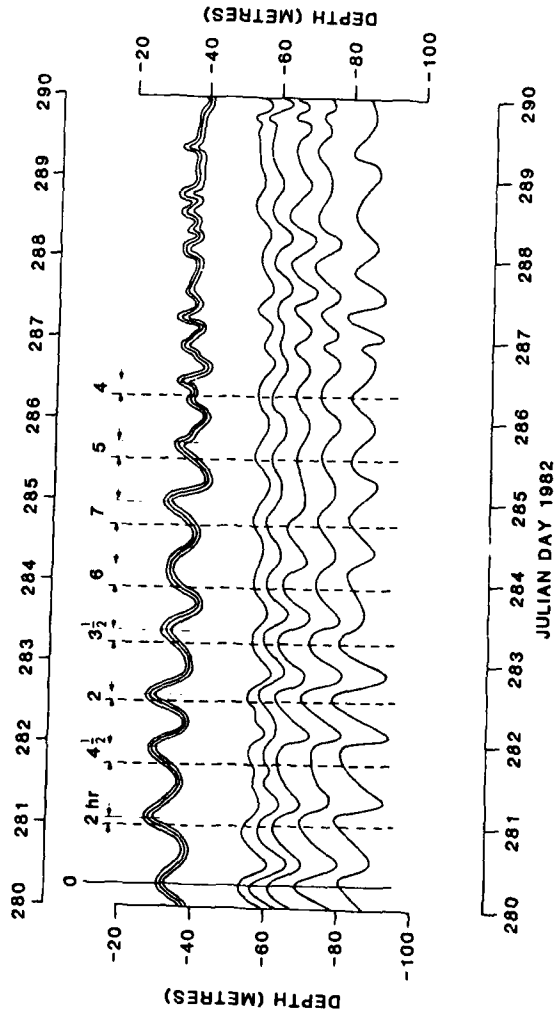
Fig. 22. Enhancement of upper and lower isotherms for days 280–290 of thermistor chain A showing the phase changes in vertical oscillations with depth.
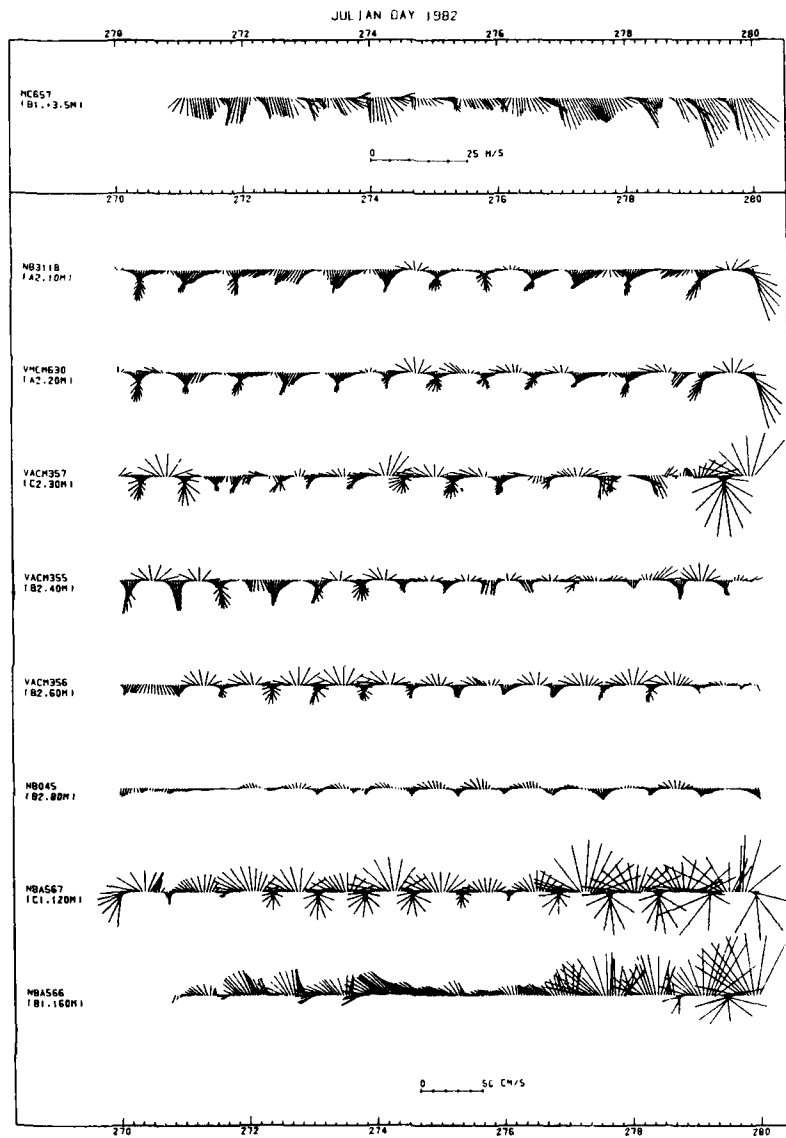
Fig. 23a. Composite stick diagram representing period JD 270–280 for all eight current-meters with depth and current-meter type indicated. The scale is indicated at the bottom of the plot. Wind sticks for the same period are plotted across the top to a different scale.
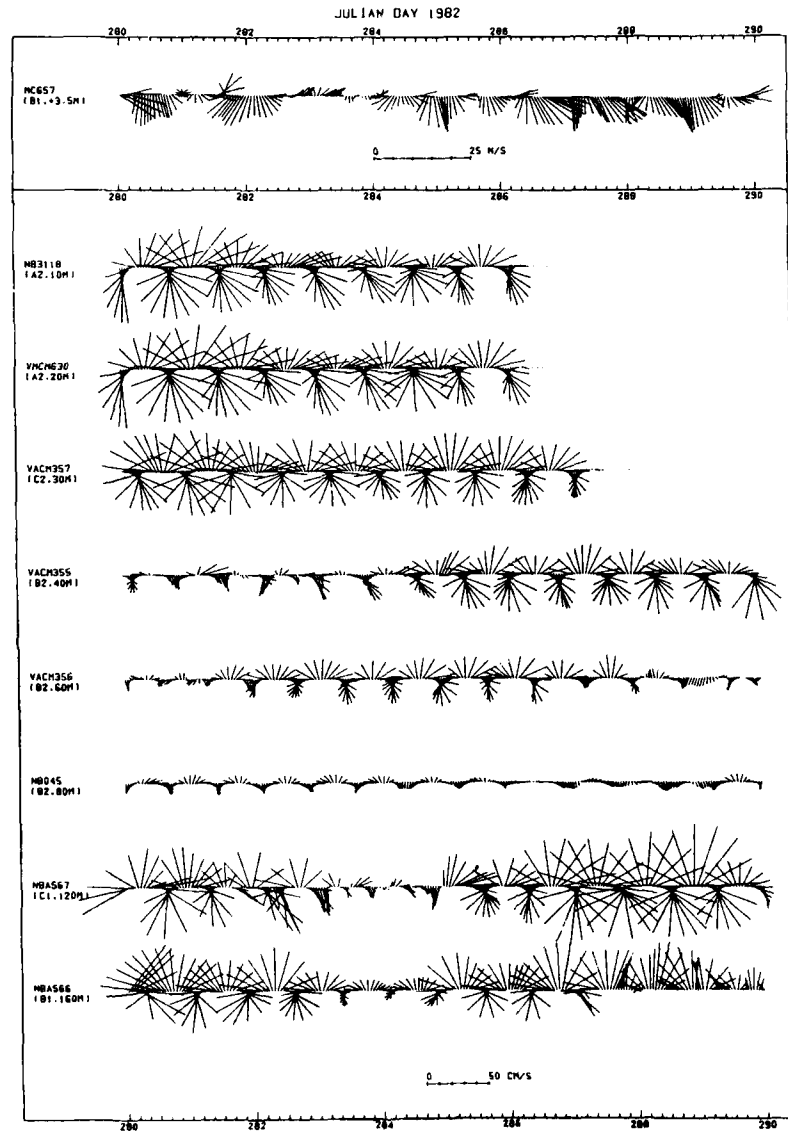
Fig. 23b. Composite stick diagram representing period JD 280-290 for current and wind vectors.
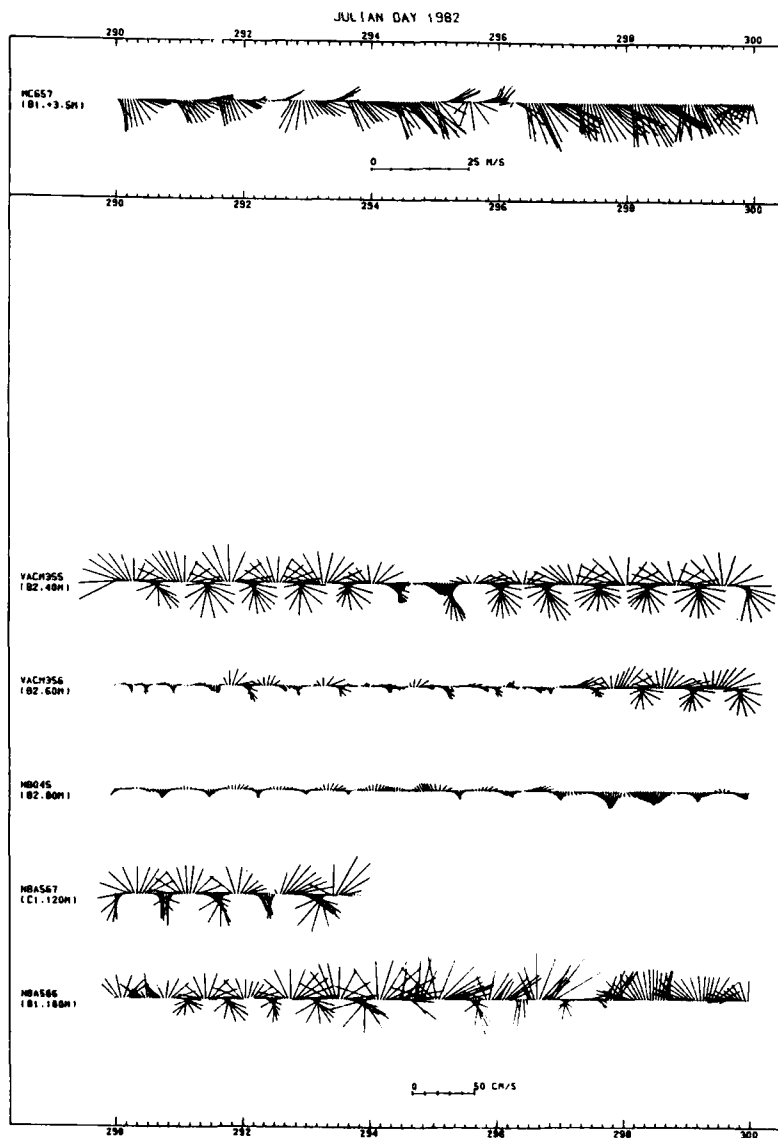
Fig. 23c. Composite stick diagram representing period JD 290–300 for current and wind vectors.
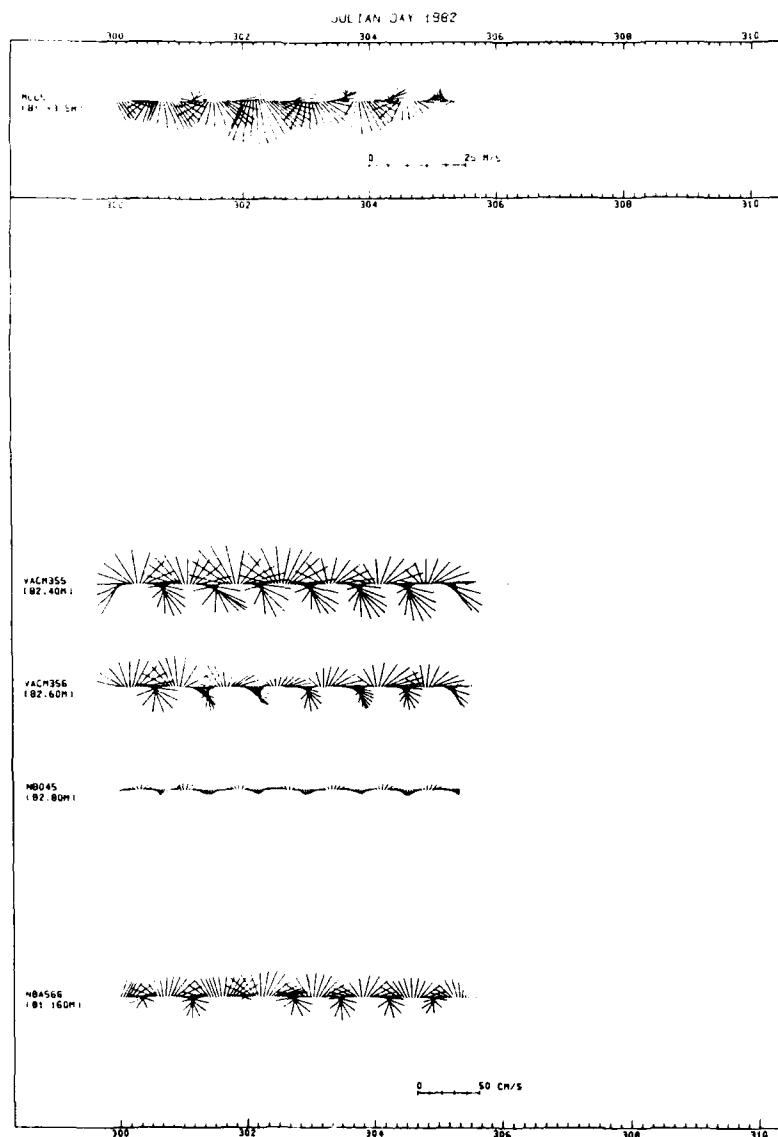
Fig. 23d. Composite stick diagram representing period JD 300-310 for current and wind vectors.
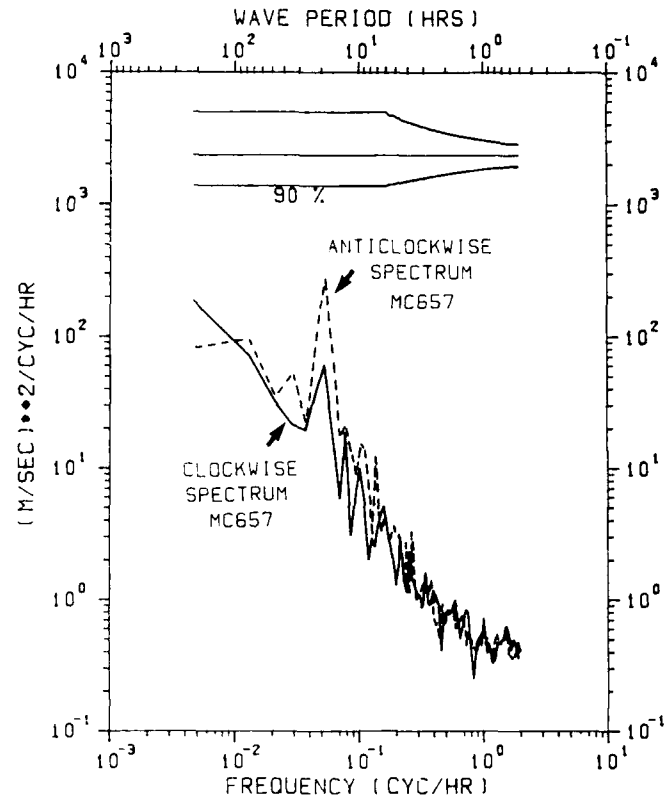
Fig. 24. Rotary spectra for wind energy at mooring B.
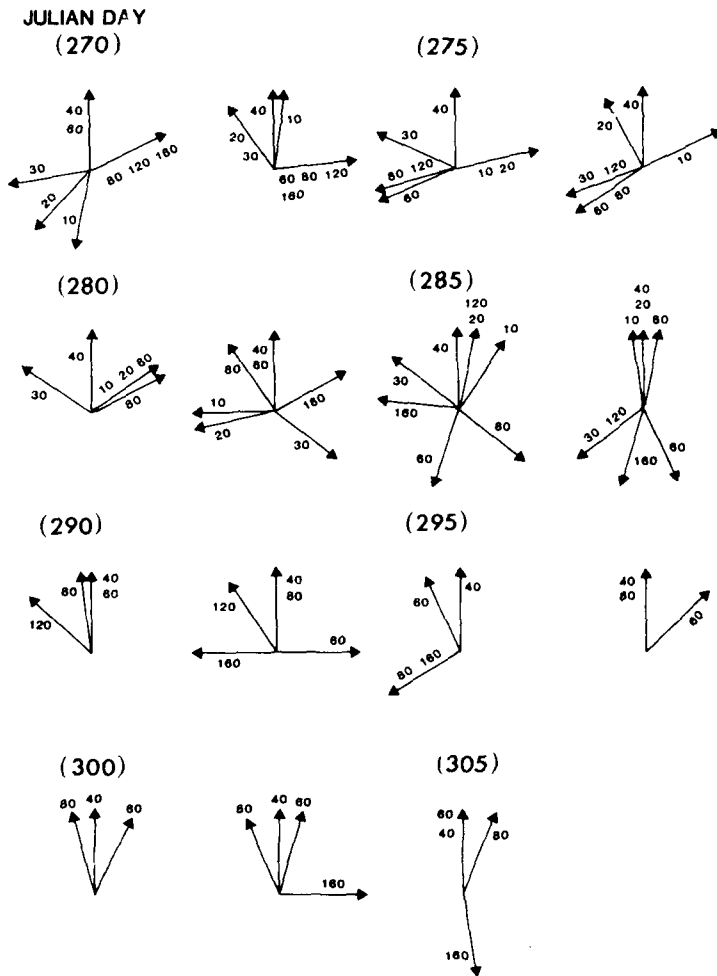
Fig. 25. Unit vectors at $2\frac{1}{2}$ intervals comparing current direction for each current meter relative to the direction at 40 m. Directions taken from Fig. 23; current-meter depth is written on each stick.

intentionally blank page
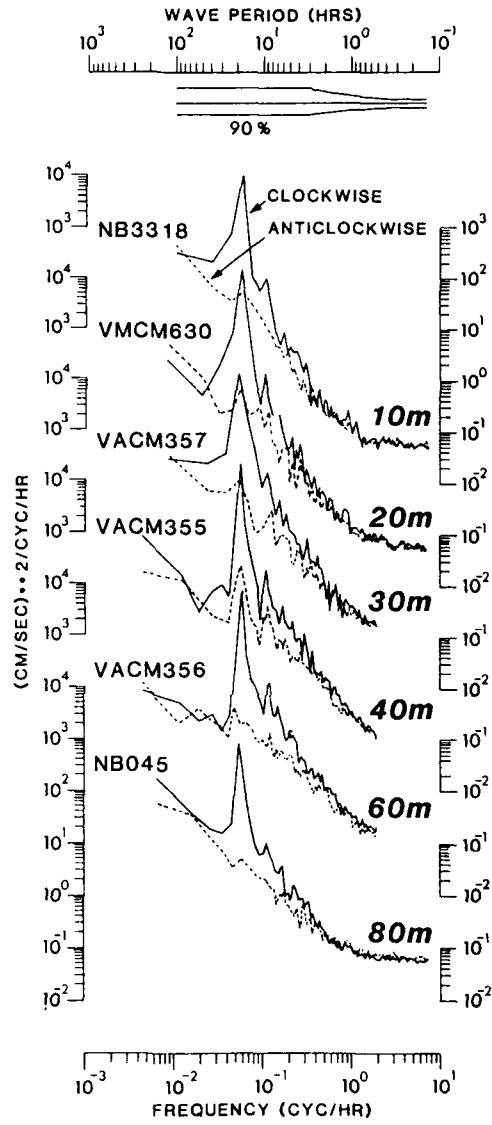
Fig. 26. Current-meter rotary spectra.
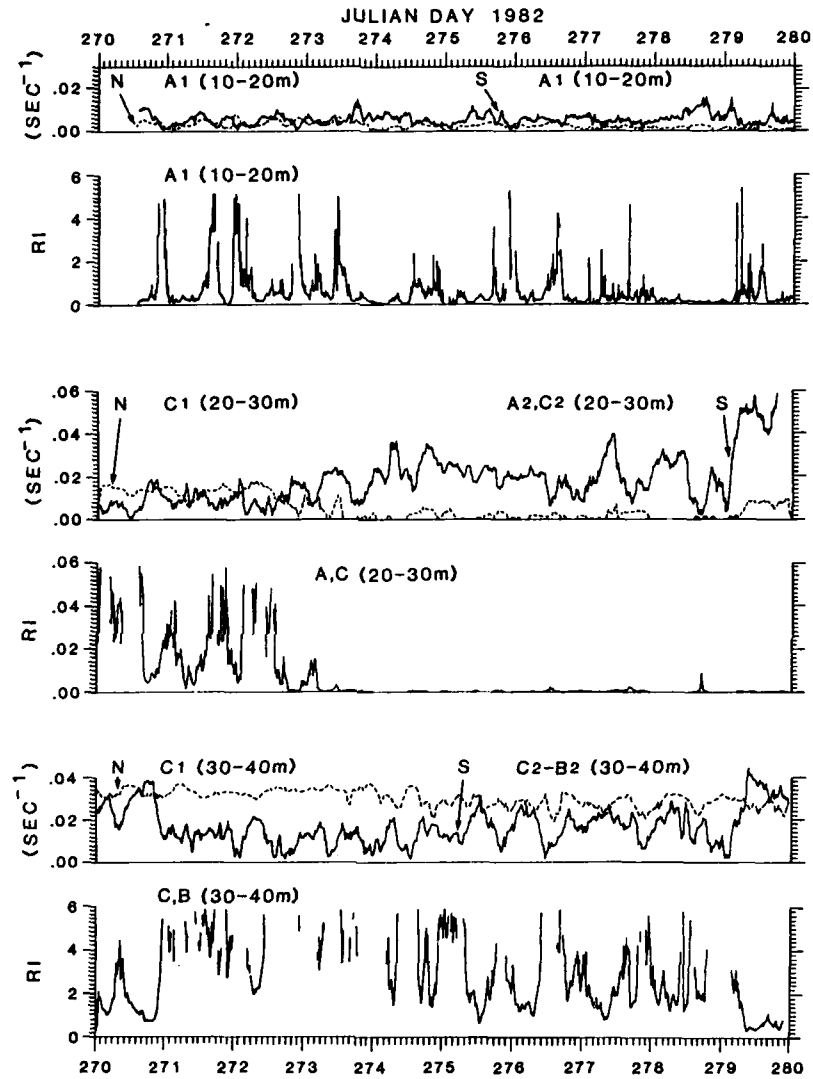
Fig. 27a. Time series plots representing period JD 270-280 of bulk estimates of Brunt-Väisälä frequency N, shear S, and gradient Richardson number Ri for depths 10-20 m, 20-30 m and 30-40 m. The mooring or moorings involved for each series is indicated, preceding the specified depth range.
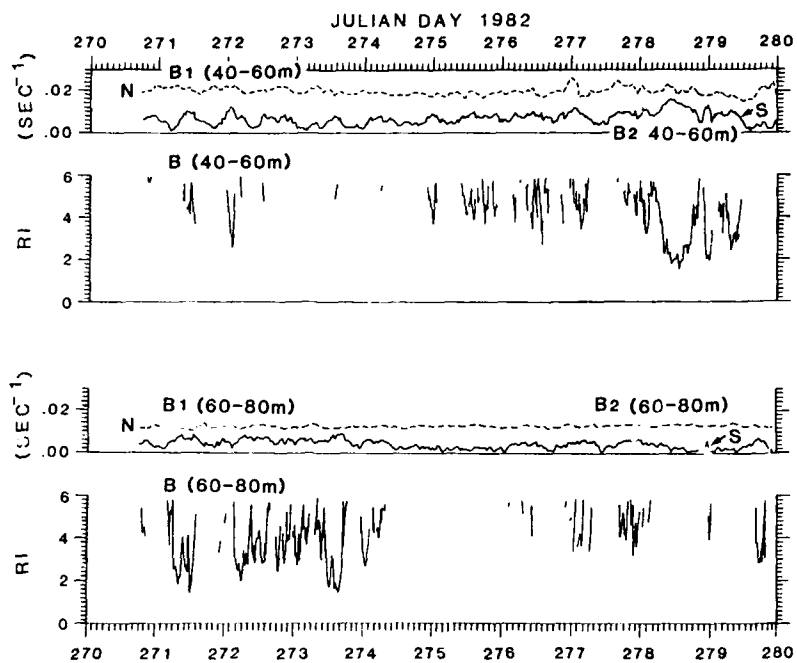
Fig. 27b. Brunt-Väisälä frequency N, shear S, and gradient Richardson number Ri for period 'D 270-280 and depths 40-60 m and 60-80 m.
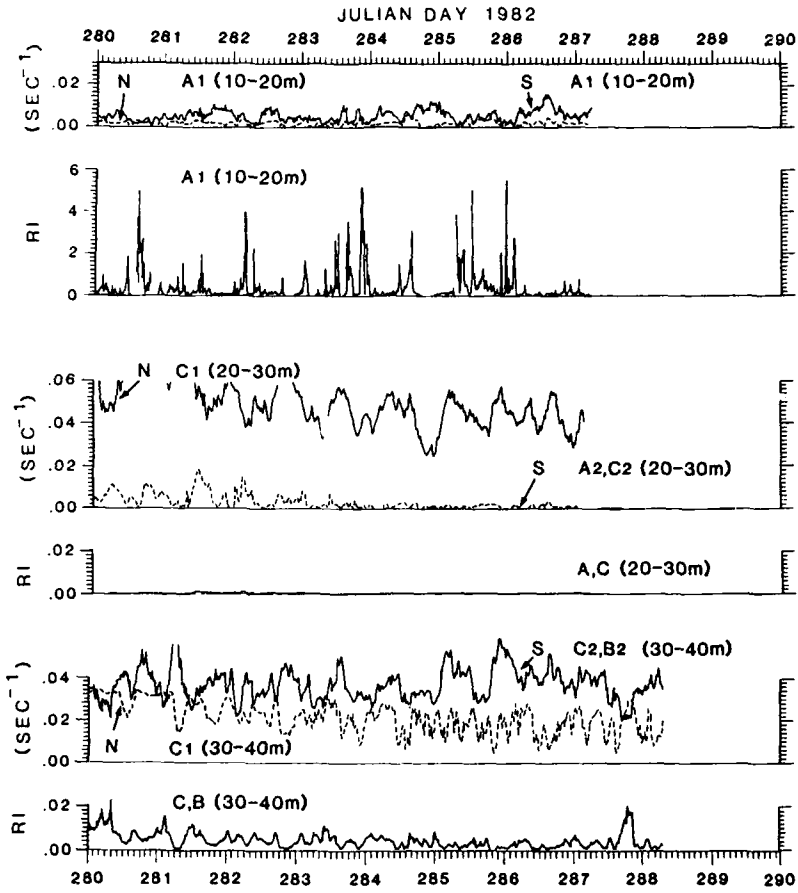
*Fig. 28*a. Time series plots representing period JD 280-290 of bulk estimates of Brunt-Väisälä frequency N, shear S, and gradient Richardson number Ri for depth 10-20 m and 30-40 m. The mooring or moorings involved for each series is indicated, preceding the specified depth range.
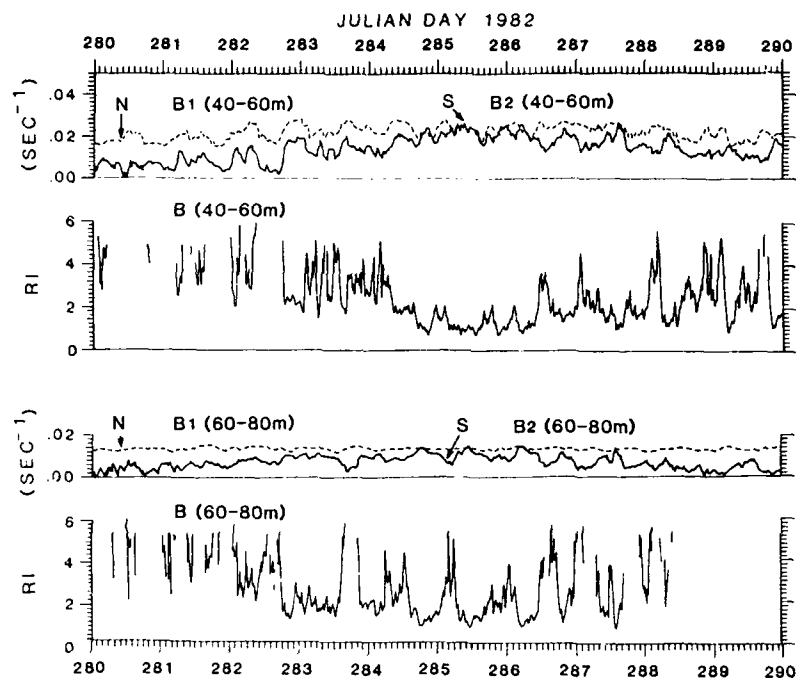
Fig. 28b. Brunt-Väisälä frequency N, shear S and gradient Richardson number Ri for period JD 280-290 and depths 40-60 m and 60-80 m.

- 39
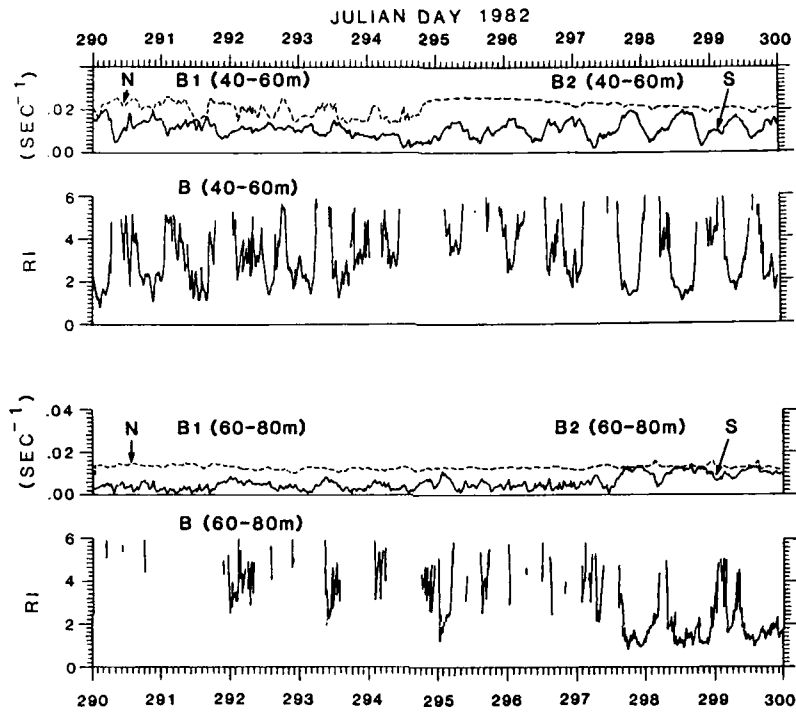
Fig. 29. Time series plots representing period JD 290-300 of bulk estimates of Brunt-Väisälä frequency N, shear S, and gradient Richardson number Ri for depth 40-60 m and 60-80 m. The mooring or moorings involved for each series is indicated, preceding the specified depth range.
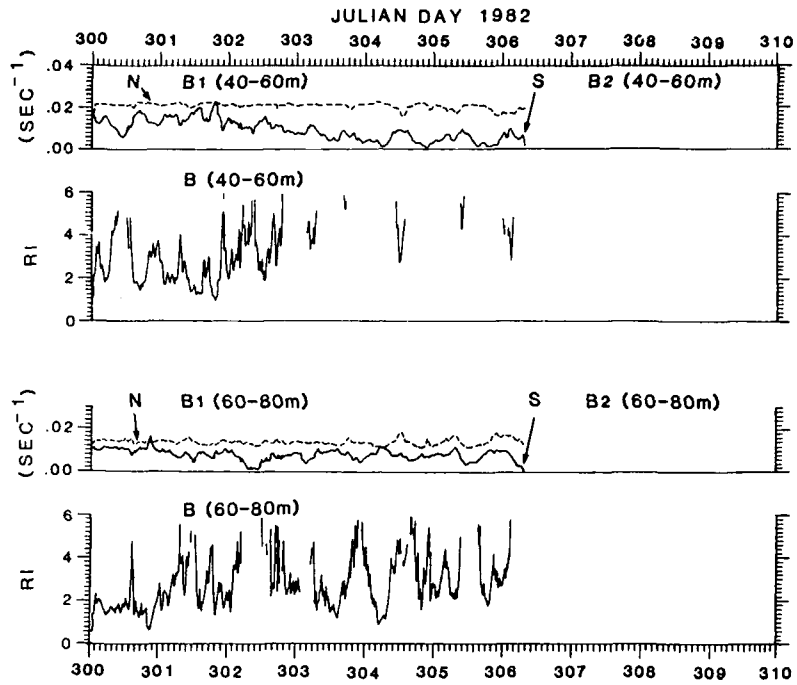
Fig. 30. Time series representing period JD 300-310 of bulk estimates of Brunt-Väisälä frequency *N*, shear *S*, and gradient Richardson number Ri for depths 40-60 m and 60-80 m. The mooring or moorings involved for each series is indicated, preceding the specified depth range.

B1
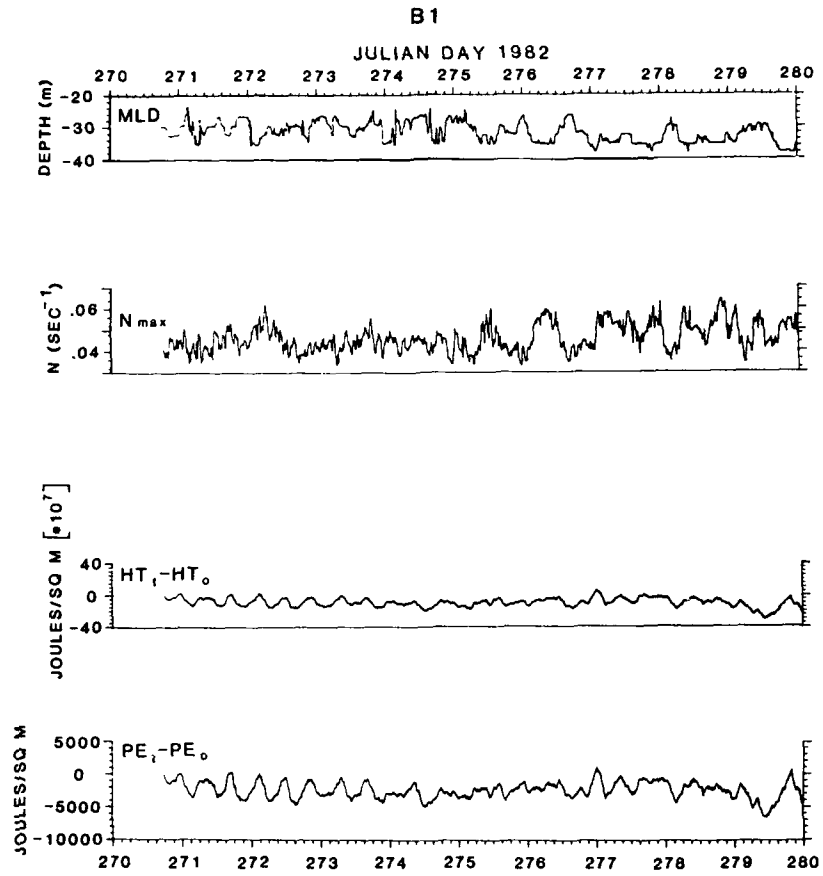
Fig. 31a. Time series plots for period JD 270-280 of mixed-layer depth MLD, maximum Brunt-Väisälä frequency Nmax, change in heat content $HTt-HTo$, and change in potential energy $PEt-PEo$. All estimates are for mooring B1.

B 1

JULIAN DAY 1982
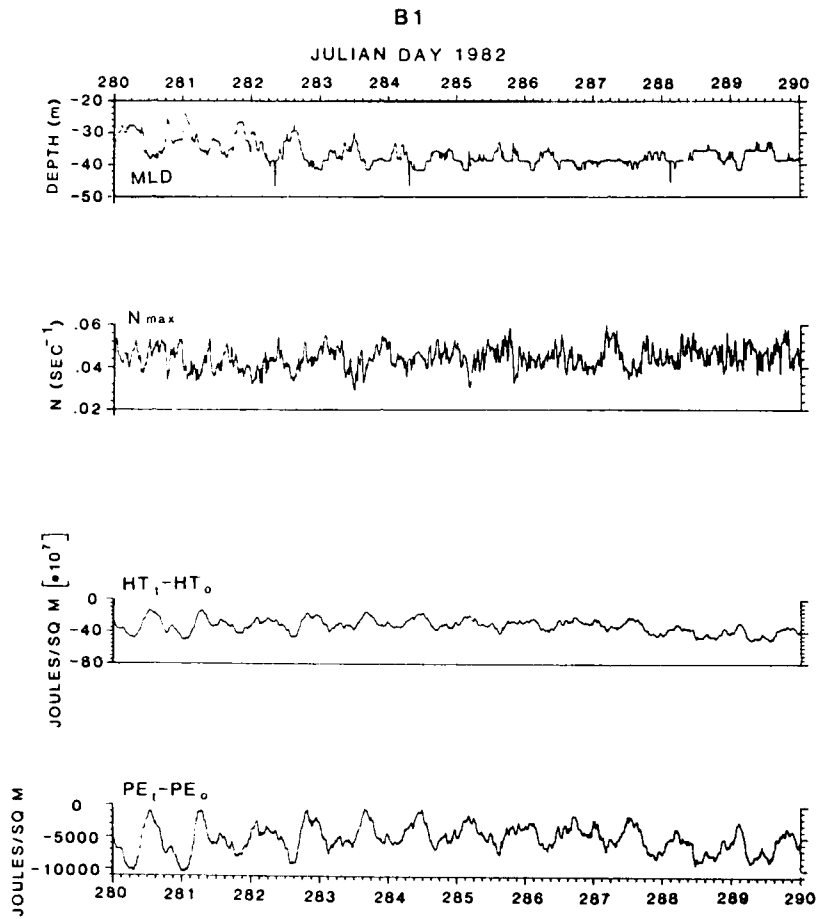
Fig. 31b. Time series plots for period JD 280-290 of mixed-layer depth MLD, maximum Brunt-Väisälä frequency Nmax, change in heat content $HTt-HTo$, and change in potential energy $PEt-PEo$. All estimates are for mooring B1.

B1
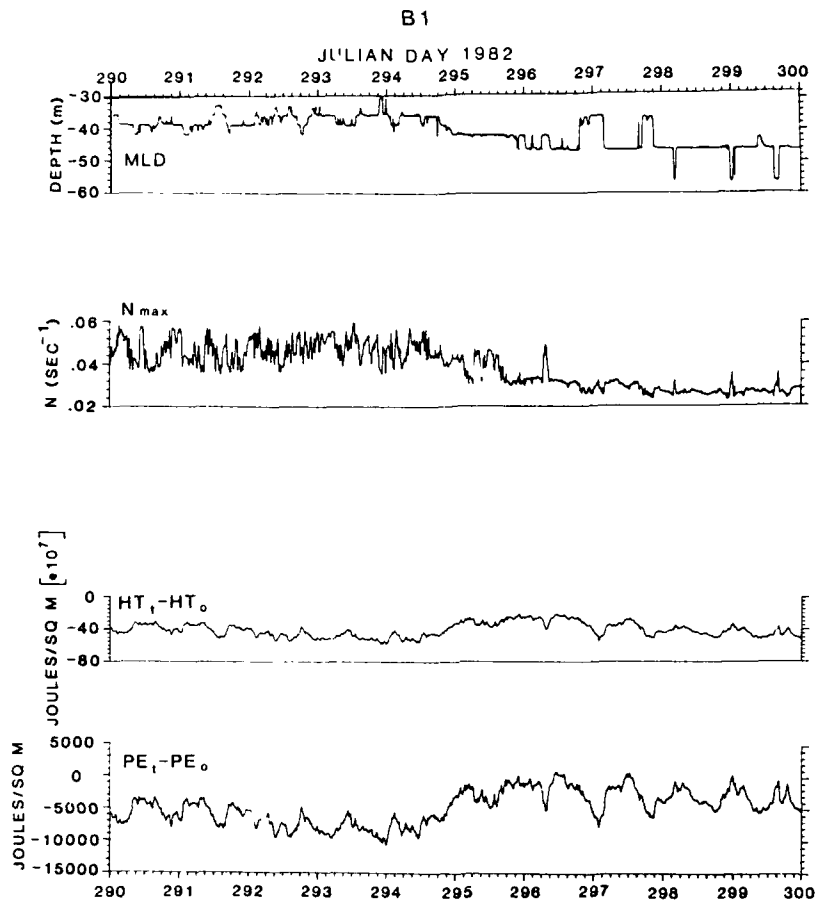
Fig. 31c. Time series plots for period JD 290-300 of mixed-layer depth *MLD*, maximum Brunt-Väisälä frequency *N*max, change in heat content *HT*t-*HT*o, and change in potential energy *PE*t-*PE*o. All estimates are for mooring B1.

B1

JULIAN DAY 1982
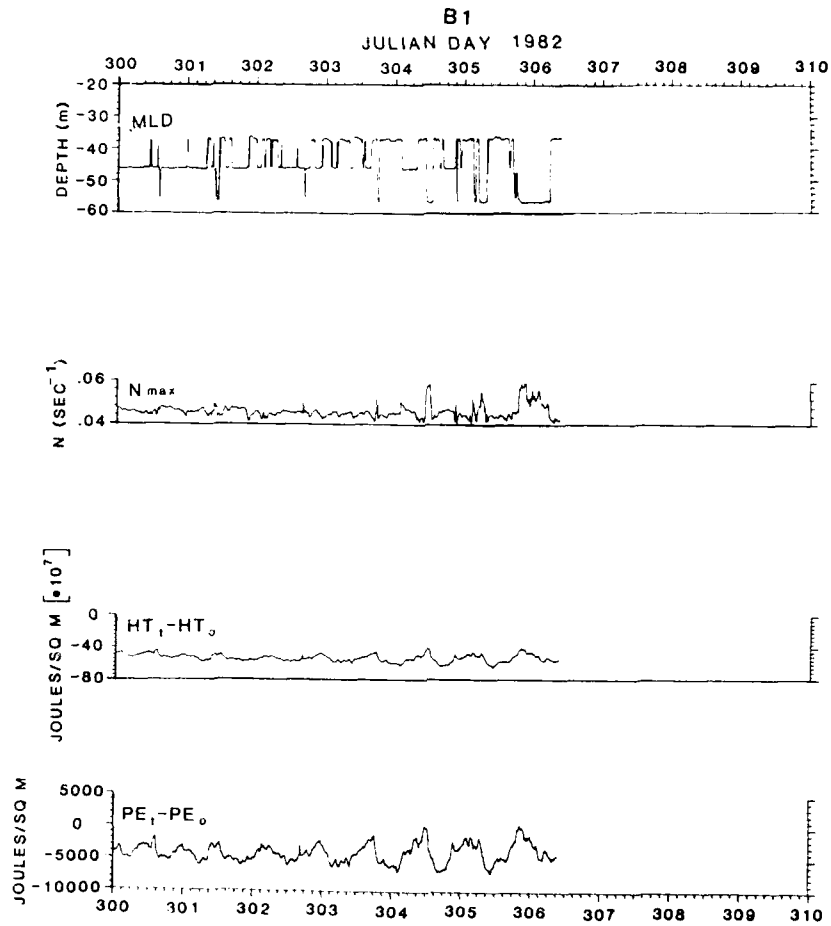
Fig. 31d. Time series plots for period JD 300-310 of mixed-layer depth MLD, maximum Brunt-Väisälä frequency Nmax, change in heat content HTt-HTo, and change in potential energy PEt-PEo. All estimates are for mooring B1.

B1

JULIAN DAY 1982
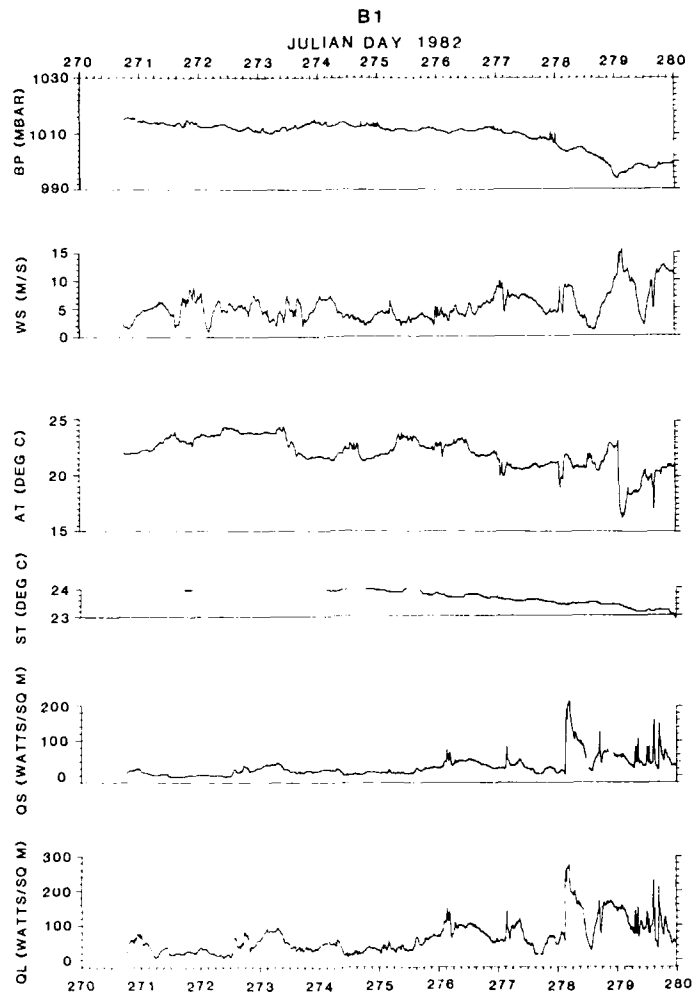
Fig. 32a. Time series plots for period JD 270–280 of barometric pressure *BP*, wind speed *WS*, air temperature *AT*, sea surface temperature *ST*, and estimates of sensible and latent heat fluxes *QS* and *QL* respectively. All estimates are for mooring B1.

B1
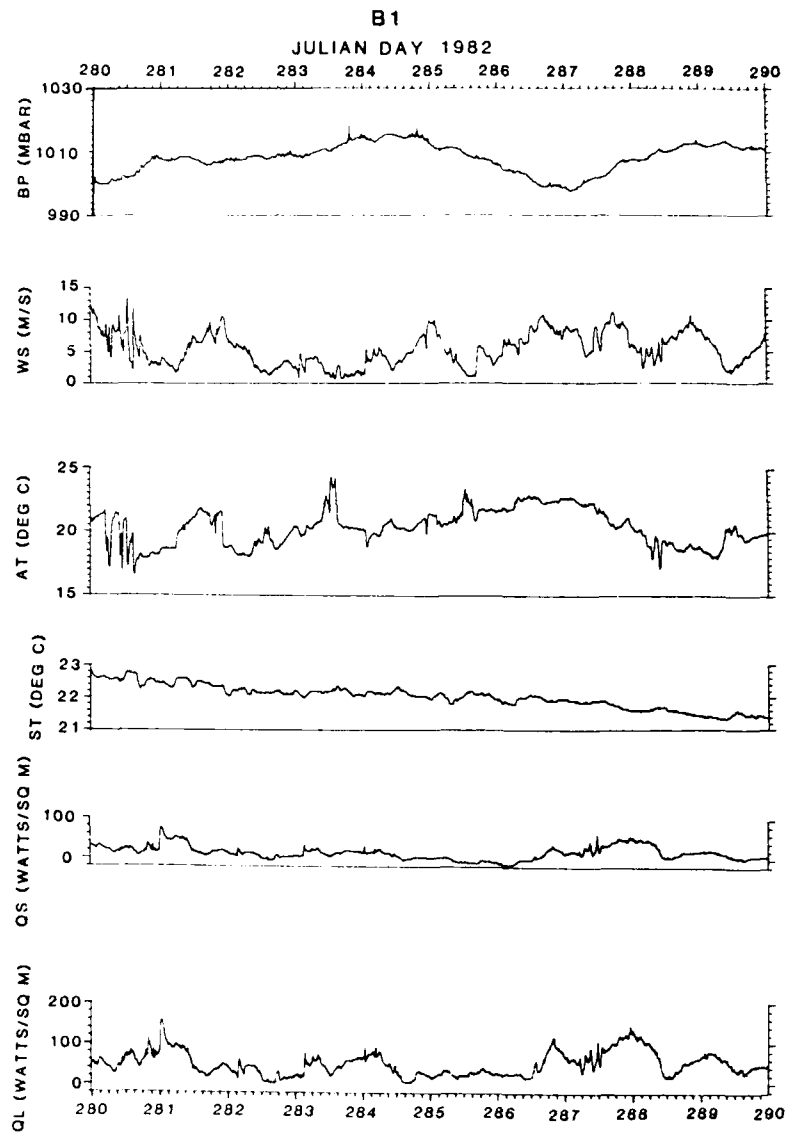
Fig. 32b. Time series plots for period JD 280–290 of barometric pressure *BP*, wind speed *WS*, air temperature *AT*, sea surface temperature *ST*, and estimates of sensible and latent heat fluxes *QS* and *QL* respectively. All estimates are for mooring B1

B1
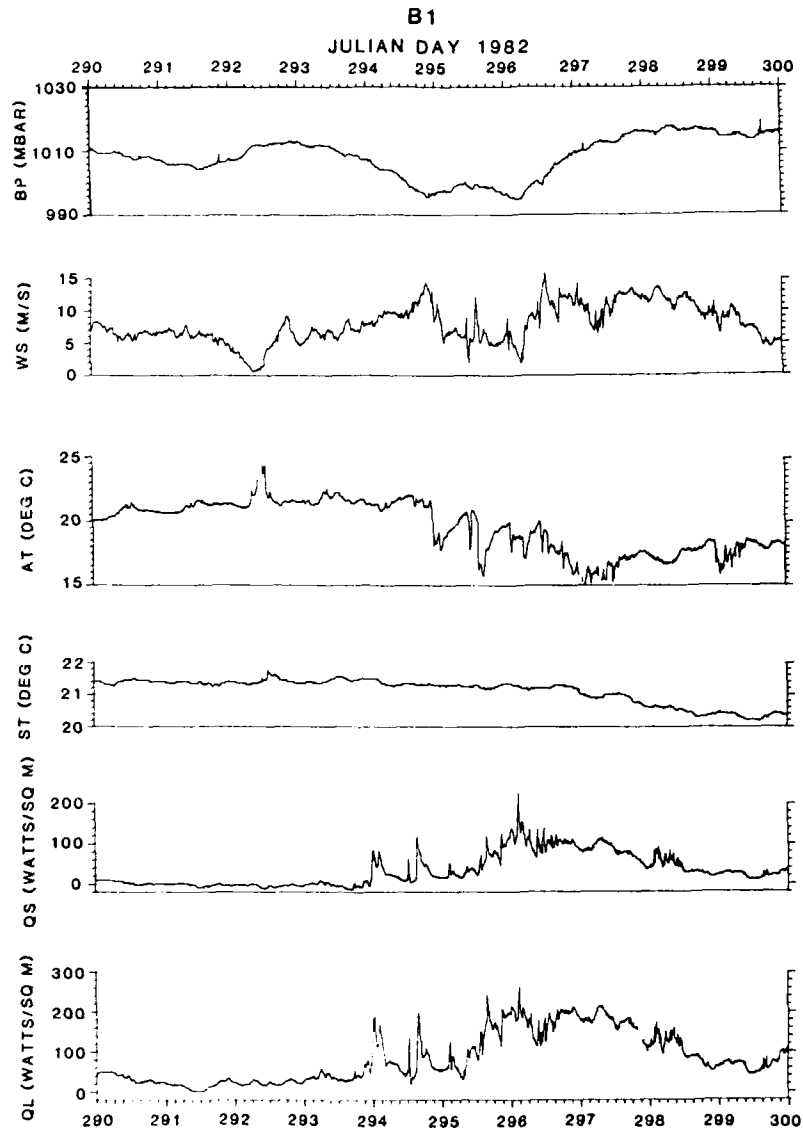
Fig. 32c. Time series plots for period JD 290–300 of barometric pressure BP, wind speed WS, air temperature AT, sea surface temperature ST, and estimates of sensible and latent heat fluxes QS and QL respectively. All estimates are for mooring B1.

B1
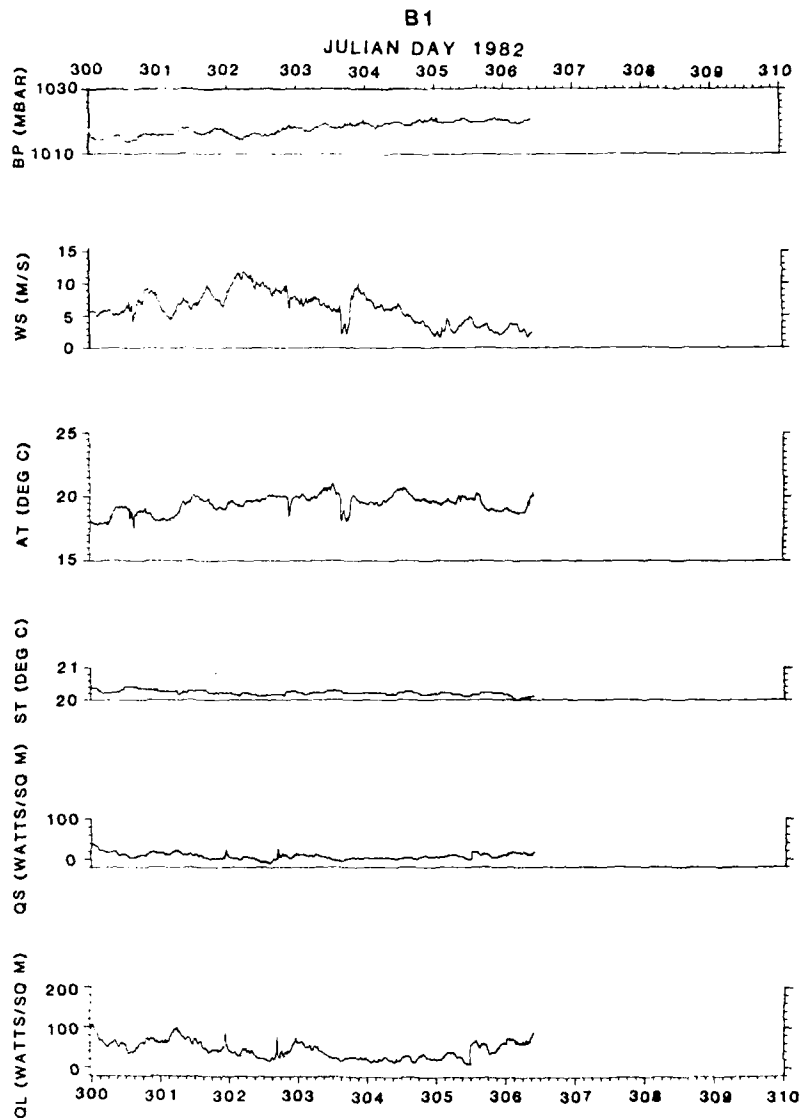
Fig. 32d. Time series plots for period JD 300–310 of barometric pressure *BP*, wind speed *WS*, air temperature *AT*, sea surface temperature *ST*, and estimates of sensible and latent heat fluxes *QS* and *QL* respectively. All estimates are for mooring B1.

Initial Distribution for SM-213

Ministries of Defence		SCNR Denmark	1
JSPHQ Belgium	2	SCNR Germany	1
DND Canada	10	SCNR Greece	1
CHOD Denmark	8	SCNR Italy	1
MOD France	8	SCNR Netherlands	1
MOD Germany	15	SCNR Norway	1
MOD Greece	11	SCNR Portugal	1
MOD Italy	10	SCNR Turkey	1
MOD Netherlands	12	SCNR UK	1
CHOD Norway	10	SCNR US	2
MOD Portugal	5	SECGEN Rep. SCNR	1
MOD Spain	2	NAMILCOM Rep. SCNR	1
MOD Turkey	5		
MOD UK	20	National Liaison Officers	
SECDEF US	60	NLO Canada	1
		NLO Denmark	1
NATO Authorities		NLO Germany	1
Defence Planning Committee	3	NLO Italy	1
NAMILCOM	2	NLO UK	1
SACLANT	3	NLO US	1
SACLANTREPEUR	1		
CINCWESTLANT/		NLR to SACLANT	
COMOCEANLANT	1	NLR Belgium	1
COMSTRIKFLTANT	1	NLR Canada	1
CINCIBERLANT	1	NLR Denmark	1
CINCEASTLANT	1	NLR Germany	1
COMSUBACLANT	1	NLR Greece	1
COMMAIREASTLANT	1	NLR Italy	1
SACEUR	2	NLR Netherlands	1
CINCNORTH	1	NLR Norway	1
CINCSOUTH	1	NLR Portugal	1
COMNAVSOUTH	1	NLR Turkey	1
COMSTRIKFORSOUTH	1	NLR UK	1
COMEDCENT	1		
COMMARAIRMED	1		
CINCHAN	3	Total external distribution	236
		SACLANTCEN Library	10
SCNR for SACLANTCEN		Stock	34
SCNR Belgium	1		
SCNR Canada	1	Total number of copies	280